ECE 445 / ME 470

SENIOR DESIGN LABORATORY

DESIGN DOCUMENT

Softbot: Jellyfish-Inspired Bionic Soft Robot with Visual Perception

---

Team #14

YINLIANG GAN
(gan10@illinois.edu)
JUNWEI ZHANG
(junweiz4@illinois.edu)
WANGJIE XU
(wangjie3@illinois.edu)
SHURAN YAN
(shurany2@illinois.edu)

TA: Jiangshan Zhuo

April 13, 2025

Contents

1 Introduction

The ocean, covering more than 70% of the Earth's surface, plays a vital role in climate regulation, resource provision, and human development, which has driven continuous exploration efforts since ancient times [1]. To support these endeavors, underwater robotic systems have emerged as essential tools by enabling access to hazardous and unstructured environments that are otherwise difficult or impossible for humans to reach [2]. At the heart of these systems lies actuation technology, which is critical to achieving effective and reliable movement. However, traditional rigid actuators, despite their high power output, often exhibit limitations such as restricted compliance, poor adaptability to complex terrains, and increased risk of mechanical failure under unpredictable conditions [3], [4]. In contrast, soft robots—while still maintaining reasonable locomotion speed—offer enhanced flexibility, compliance, environmental adaptability, and biocompatibility, making them inherently safer for interaction with living organisms [5]. These unique advantages have revitalized the development of actuation systems for underwater exploration, positioning soft robotics as a promising direction in the field.

Current soft actuator technologies include dielectric elastomer actuators (DEAs), hydraulically amplified self-healing electrostatic (HASEL) actuators, and other mechanisms that emphasize compliance, adaptability, and safe interaction [6]. DEAs, which operate by deforming in response to electrostatic forces between two electrodes, were first demonstrated as artificial muscles by Pelrine et al. [7] in 2000. DEAs offer high efficiency, large force output, and flexibility. Researchers have utilized these excellent properties to create fish-shaped deep-sea robots capable of withstanding high water pressure, as well as jellyfish-shaped untethered transparent robots [8], [9]. However, DEAs are limited in deformation capability and lack self-healing properties due to their solid dielectric materials [10]–[12]. In contrast, HASEL actuators overcome these limitations by using liquid dielectrics, which not only enable larger deformations but also offer self-healing capabilities [13]–[15]. This allows HASEL actuators to achieve muscle-like motion with rapid response, high efficiency, and a favorable power-to-weight ratio, significantly enhancing long-term reliability [16], [17]. A notable example is the Ocyropsis-inspired robot, which combines electro-hydraulic actuation with a rowing mechanism to achieve high-speed swimming and dexterous movement in underwater environments. It can reach speeds of 1.1 body lengths per second while maintaining low power consumption and high durability [18]. However, despite these advantages, HASEL actuators still face challenges such as limited force output and specific power. Moreover, efforts to improve performance—such as reducing electrode spacing and employing high-dielectric materials—often increase the risk of dielectric breakdown, thereby compromising their reliability and operational safety [19], [20]. Given the complementary strengths of DEAs in control precision and HASELs in deformation and self-healing, a hybrid actuation strategy that integrates both offers a compelling pathway forward—particularly for applications requiring both fine manipulation and large, adaptive motion.

In underwater robotics, effective control is essential for navigating dynamic and unstructured environments [21]. Reinforcement learning (RL) has gained popularity for enabling robots to adapt and learn optimal policies for tasks like motion planning and path-

following in such environments [22], [23]. RL algorithms, including deep Q-networks (DQN) and proximal policy optimization (PPO), allow robots to improve performance over time without relying on pre-programmed models [24], [25]. In addition, external visual perception, using cameras to track the robot's position, provides critical real-time feedback for control adjustments, enhancing precision and adaptability, especially in underwater settings where visibility and conditions are constantly changing [26], [27].

In this study, we propose a hybrid actuation system called electrohydraulic bent-to-straight actuators (EBSAs), which combine dielectric elastomer actuators (DEAs) and HASEL actuators to leverage the strengths of both technologies. By integrating the precise controllability of DEAs with the large, compliant deformation of HASEL actuators, our system enhances locomotion and environmental adaptability for underwater soft robots. Two EBSAs arranged laterally form a semi-circular configuration, creating a two-dimensional bionic jellyfish robot (2D-BJR). Independent movement of each EBSA allows for steering, while synchronized movement enables rapid forward propulsion. Building on this, we developed a physical model for the robot's motion in water. Using reinforcement learning for simulation training, and combining visual perception for position tracking and body posture analysis, we have constructed a bionic jellyfish robot system capable of swimming along a predefined path within a plane.

1.1 Problem Statement

The vast ocean is essential for climate regulation, resource provision, and human development. However, exploring and navigating this complex and unpredictable environment remains a significant challenge. Traditional rigid actuators, despite their high power output, are limited in flexibility, compliance, and adaptability, which hinders their performance in the dynamic underwater environment. These actuators are prone to mechanical failure, especially in unstructured terrains, making them less suited for underwater applications [3], [4]. Soft actuators, such as dielectric elastomer actuators (DEAs), offer high efficiency and flexibility, but their performance is constrained by limited deformation and lack of self-healing capabilities, due to the solid nature of their dielectric materials [10]–[12]. In contrast, HASEL actuators overcome some of these limitations by using liquid dielectrics, which allow for larger deformations and self-healing behavior [13]–[15]. However, HASEL actuators still struggle with limited force output and specific power, which limits their full potential for underwater robotics [19], [20].

To navigate these challenges, effective control strategies are as crucial as actuators. Reinforcement learning (RL) has shown promise in enabling robots to adapt to complex, dynamic environments, making it a valuable tool for motion planning, path-following, and decision-making [22], [23]. However, integrating RL-based control with actuation systems, while maintaining high precision and real-time adaptability in underwater environments, remains a significant challenge [24], [25].

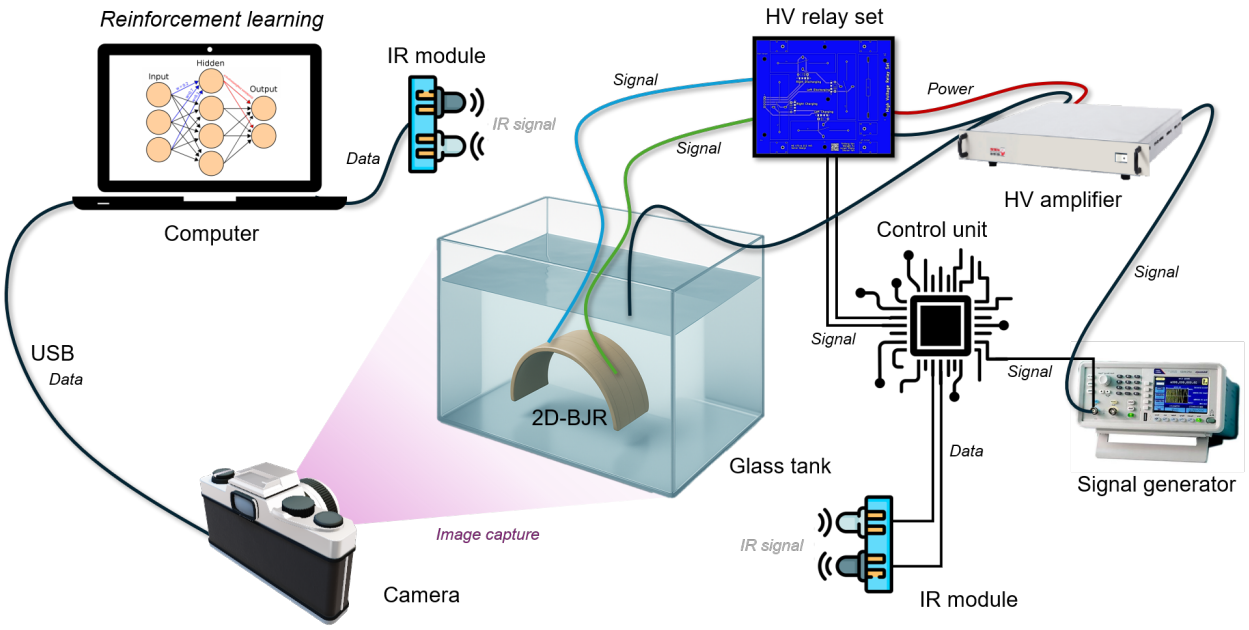

Figure 1: Visual aid of 2D-BJR system

1.2 Solution Overview

In this study, we present a hybrid actuation system for underwater robots, combining dielectric elastomer actuators (DEAs) and HASEL actuators. This hybrid system integrates the precise control of DEAs with the large, compliant deformation of HASELs, improving locomotion and adaptability in the 2D-BJR system. The robot's movement is guided by a predefined trajectory, which is generated through motion planning software on a host computer. This trajectory serves as a reference for comparison with the actual movement of the robot, ensuring accurate path-following.

As depicted in Figure 1, the comparison process involves capturing real-time images of the 2D-BJR system using a camera. The images are processed by a visual network to extract key parameters such as position, velocity, and orientation of the jellyfish. These parameters are then compared with the predicted trajectory, which is generated by a reinforcement learning-based physical model. Based on this comparison, the system generates optimal motion commands, which are transmitted via infrared signals to the control system. Upon receiving these commands, the control unit regulates the high-voltage relays to execute the required movement, enabling the 2D-BJR to follow the predefined path with precision and adapt to the dynamic underwater environment.

1.3 High-Level Requirements List

Here are three measurable characteristics to evaluate the solution:

- The actuator must provide competitive strong force feedback while maintaining a stable structure, demonstrating higher efficiency and adaptability compared to existing soft actuators.

- The robot's visual processing system should be capable of recognizing and responding intelligently to environmental input, facilitated by the integration of a visual perception network.
- With the utilization of reinforcement learning control algorithm, the robot system must be able to plan a path consisting of point sets, and then be controlled by the RL agent to reach the target point along a series of planned points.

2 Design

2.1 Physical Diagram

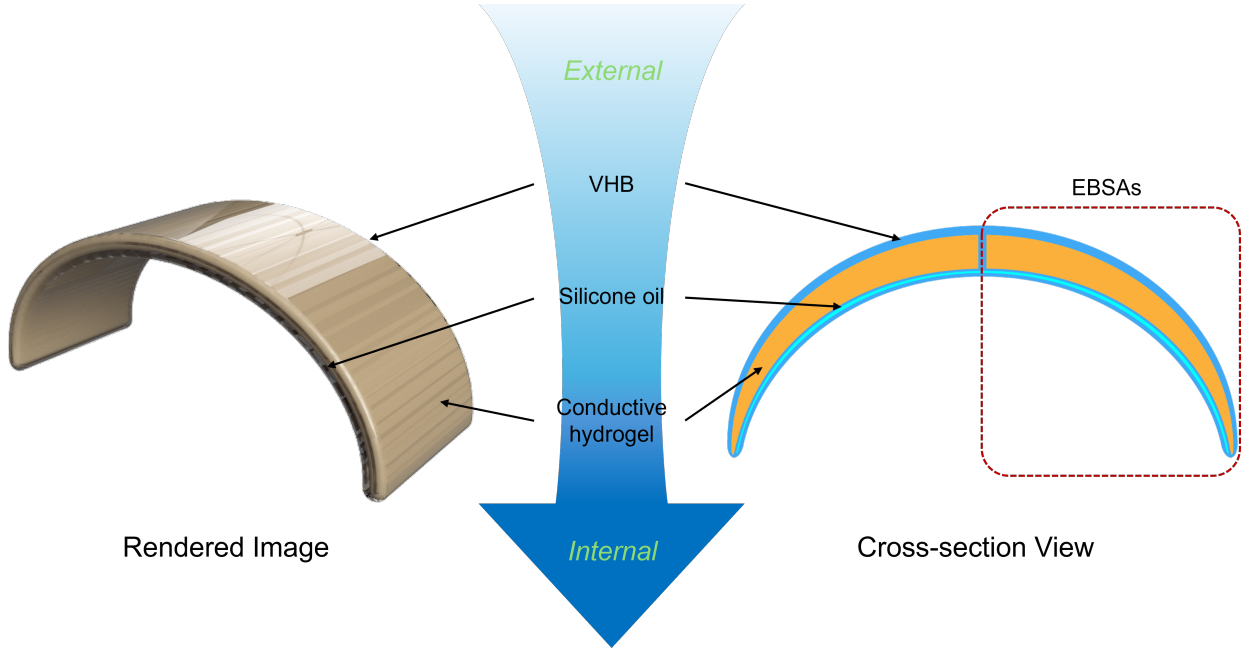

Figure 2: Rendered image and cross-sectional view of 2D-BJR. The robot has two EBSAs, which consist of Very High Bond (VHB), silicone oil and conductive hydrogel.

As illustrated in Figure 2, the mechanical structure of our senior design project adopts a cylindrical configuration formed by a semicircular arc, which effectively constrains the 2D-BJR's motion to a two-dimensional plane. To enable planar locomotion in arbitrary directions, an EBSA is integrated on each lateral side of the structure.

In addition to the mechanical subsystem, the complete physical implementation of the design comprises several essential components: a glass tank to provide the aquatic environment, a control module for the 2D-BJR, a high-voltage (HV) power supply module, and a computer system responsible for motion recognition and trajectory planning.

2.2 Block Diagram

As illustrated in Figure 3, the complete operational workflow of our senior design project is presented. Prior to each activation of the 2D-BJR system, a predefined motion trajectory for the jellyfish must be generated using a robot motion planning program on a host computer. The planned trajectory is then transmitted to the computing node, where it serves as a reference for comparison with the jellyfish's actual movement.

The comparison process proceeds as follows: a camera captures real-time images of the 2D-BJR system, and a visual processing network subsequently extracts the jellyfish's position, orientation, and velocity. These parameters are then compared with the predicted

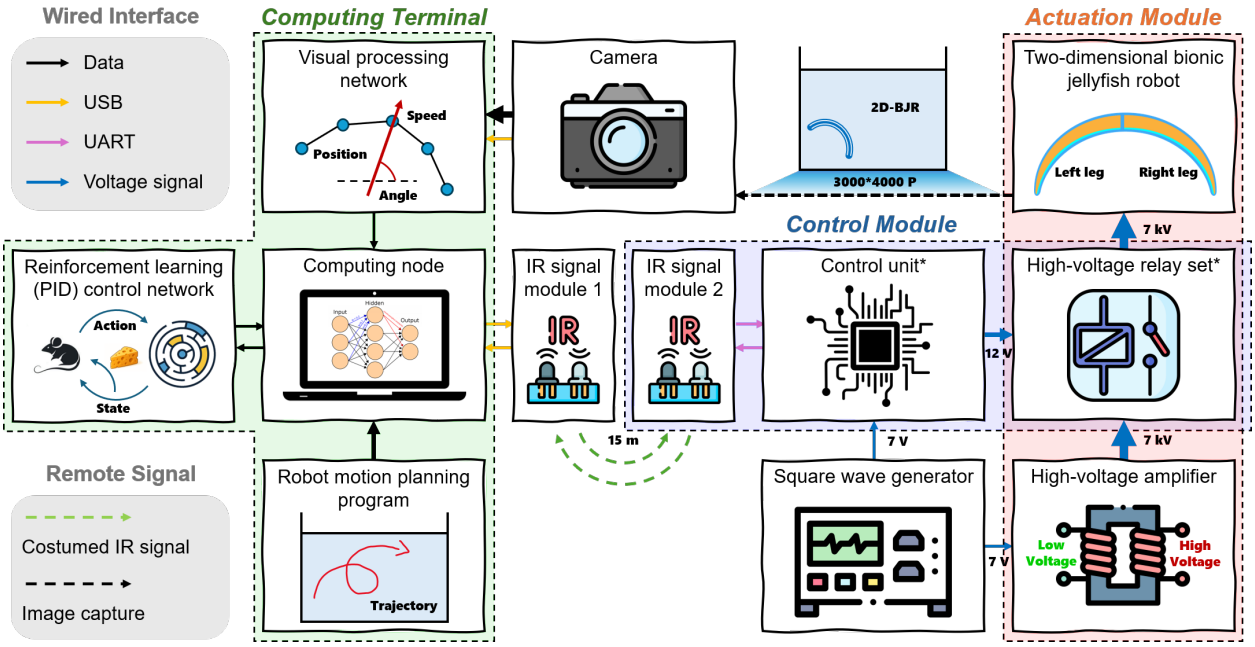

Figure 3: Block diagram of our senior design.

trajectory generated by a reinforcement learning-based physical model to determine the optimal subsequent motion.

The resulting motion command is decoded and transmitted via infrared signals. Upon receiving the signal, the infrared module within the control system decodes it and forwards the command to the control unit. Finally, the control unit regulates the switching of the HV relays, thereby inducing the desired movement of the 2D-BJR.

2.3 Computing Terminal

The computing terminal integrates data from trajectory planning, visual feedback, and control algorithms to generate remote control signals.

2.3.1 Visual Processing Network

To enable robust visual tracking of multiple soft-bodied underwater agents, such as jellyfish-inspired hydrogel robots, we adopt a modular multi-object tracking (MOT) pipeline, as illustrated in Figure 4. The system is designed for general-purpose object tracking in dynamic environments and incorporates both motion and appearance cues to improve tracking continuity.

The pipeline begins with **object detection**, where bounding boxes are extracted from each input frame using a pretrained detector (e.g., YOLOv8). These detections are then processed through two main branches: a **motion-based tracking path** and an **appearance-based association path**.

For motion modeling, we apply **Camera Motion Compensation (CMC)** to reduce the influence of platform movement or water-induced drift, followed by a **Kalman Filter**-based motion predictor integrated within the OC-SORT tracker. This enables temporal prediction of each object's location across frames.

Simultaneously, the appearance features of each detection are extracted via a **Re-Identification (ReID)** module, which can be enhanced through **Domain Adaptation (DA)** techniques to accommodate underwater image variability (e.g., lighting, turbidity). These appearance embeddings are fused with the motion predictions in an **Affinity Weighting (AW)** module.

The final association step constructs a **cost matrix** that combines motion and appearance affinity scores. A **linear assignment solver** (e.g., Hungarian algorithm) is then used to associate detections with existing tracks, yielding consistent object identities over time.

This modular design allows the framework to be adapted to various underwater scenarios, where object deformation, occlusion, and visual ambiguity are common. It supports robust tracking of soft robots without relying on rigid body assumptions, making it suitable for naturalistic or bio-inspired robotic systems.

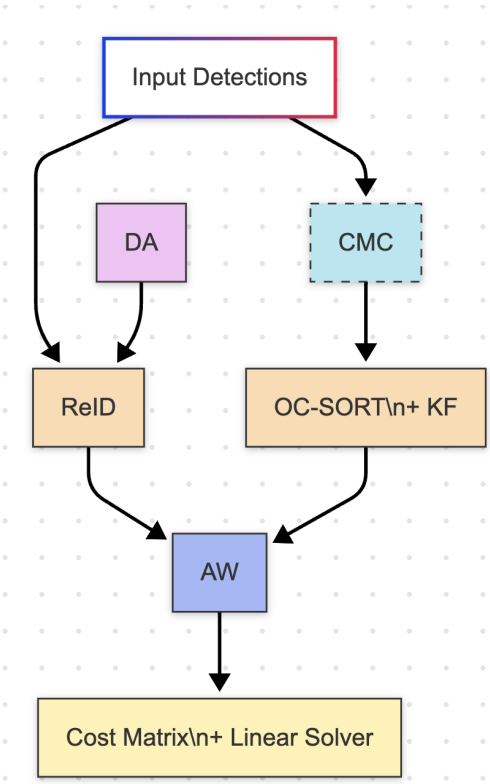

Figure 4: Visual tracking diagram.

Figure 5 presents a schematic overview of the YOLOv8 architecture, comprising a sequence of modular components designed for efficient and accurate object detection. The

network begins with an **Input** image, typically of resolution $640 \times 640 \times 3$, which is processed through an initial **Convolutional (Conv)** layer for basic feature extraction.

Subsequently, the architecture employs the **C2f** module, a computationally efficient feature extraction block introduced in YOLOv8. This module integrates residual connections and a cross-stage partial structure to enhance feature reuse and reduce redundancy. To further enrich the receptive field, the model incorporates the **Spatial Pyramid Pooling – Fast (SPPF)** module, which facilitates multi-scale feature aggregation via successive max-pooling operations.

A second **C2f** layer is utilized to refine the high-level semantic features before passing them to the **Detection Head**. The **Detect** module outputs dense predictions including bounding box coordinates, objectness scores, and class probabilities.

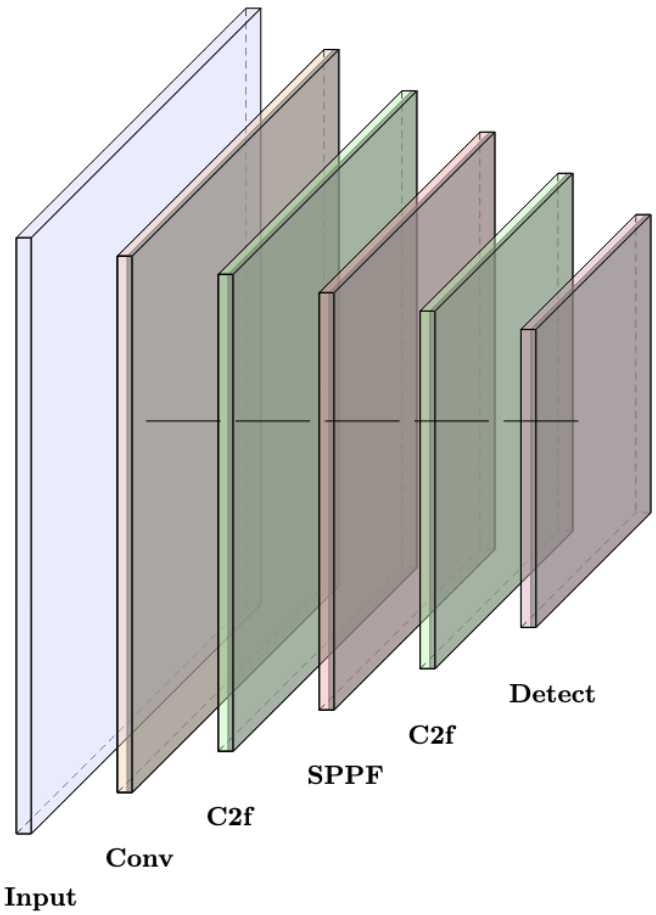

Figure 5: Yolov8 structure diagram.

Table 1: Requirements and verification table for visual processing network.

Requirements	Verification
1. The visual processing module must be able to process input data at a rate of 30 fps or higher. 2. The accuracy of the five recognition points' position must be above 95%.	1. A. Conduct performance testing at various frame rates, ensuring the module maintains $\geq$30 fps. B. Create a checklist to confirm that every test run achieves the frame rate requirement. C. Analyze performance logs to ensure there are no frame drops. 2. A. Use statistical sampling methods to test recognition point accuracy. B. Conduct a series of tests to confirm that each point maintains 95% accuracy.

2.3.2 Computing Node

The **computing node** serves as the central hub for data aggregation, exchange, and algorithmic computation. This system, which will be deployed on a high-performance laptop, processes the full workflow from video signal input to recognition, control calculations, and ultimately outputs control signals to the control unit. In addition, the computing node will support the full lifecycle of jellyfish control, providing real-time detection and visualization of operation data.

The data flow within the computing node is shown as in Figure 6. The node begins by receiving **video input**, which is captured by a camera. The video data is then processed by the **YOLO (You Only Look Once)** model, an advanced object detection system. The visual perception system analyzes the video frames to identify objects, such as obstacles or features relevant to navigation or control. After the objects are identified, the **path planning** module is triggered. This step calculates the optimal movement or path based on the objects detected in the video. The **Reinforcement Learning (RL)** module integrates reinforcement learning techniques to refine the decision-making process. It adapts the control strategy based on the position and posture provided by visual perception module and target points sequence provided by the path planning module, enhancing the system's ability to make intelligent decisions. All of the data will be process to enable the visualization of the process. And the results will be shown on the screen. Finally, the control signals generated from the RL module are sent to the **RC-sender**. This device communicates the finalized commands externally to the control unit through the **Universal Asynchronous Receiver/Transmitter (UART)** protocol, enabling precise remote control.

In essence, this system processes real-time video data, performs object detection, calculates optimal paths, refines decisions using reinforcement learning, and sends the final control signals to the control unit for execution.

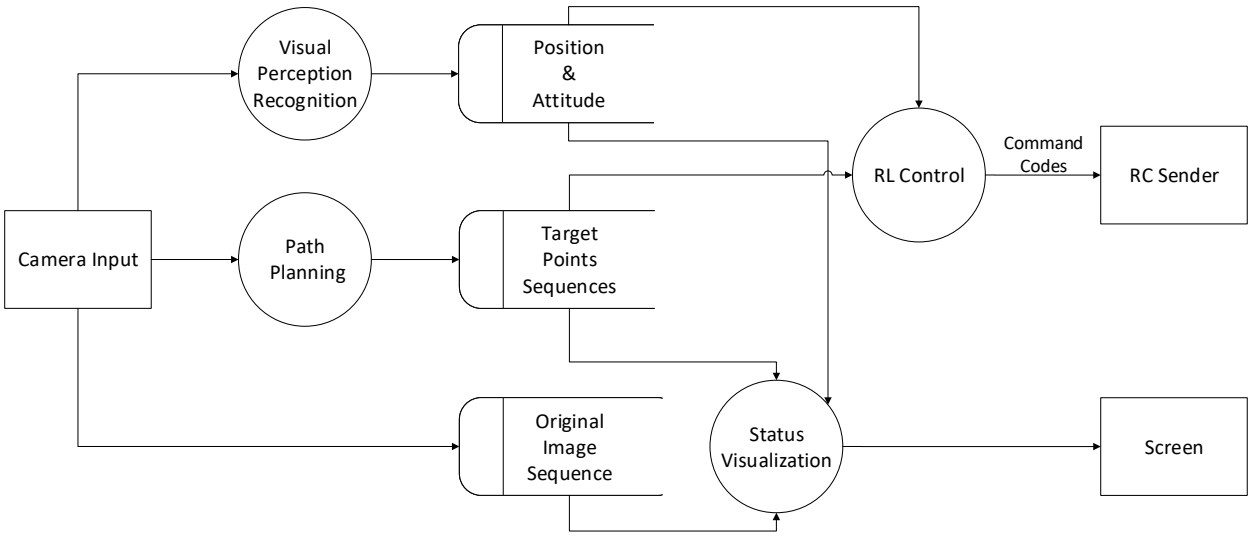

Figure 6: Data flow diagram of the computing node.

Table 2: Requirements and verification table for computing node.

Requirements	Verification
1. The computing node must facilitate data exchange and algorithm computation. 2. The delay from a single frame camera input to the transmitted signal must be within 200 ms.	1. A. Connect peripherals (including the camera and IR signal module) to the computing device (a laptop). B. Start the jellyfish control system. Check if the video signal can be received, if the vision module can output recognition points in real time, if the RL system can read the values and provide control signals, and if the RC transmitter is flashing (indicating that it is transmitting signals). 2. A. Launch the system testing tool we developed. Record the time of signal output for over ten individual tests. B. Calculate the maximum and average recorded times. If both are less than 200 ms, the test is considered successful.

2.3.3 Reinforcement Learning Control Network

For the motion control of the jellyfish model, we will adopt a deep reinforcement learning (RL) approach. Deep reinforcement learning (DRL) is a combination of reinforcement learning (RL) and deep learning. In RL, an agent interacts with an environment and

learns to take actions that maximize a cumulative reward [28]. The learning process is typically governed by the Bellman equation, which is:

$$Q^*(s,a) = \mathbb{E}[r + \gamma \max_{a'} Q^*(s',a')] \tag{1}$$

Where $Q^*(s,a)$ is the optimal action-value function. r is the immediate reward. γ is the discount factor. s' is the next state, and a' is the next action.

In this project, since the control action output is binary in nature (two-bit binary encoding), we will use the Proximal Policy Optimization (PPO) algorithm, which performs excellently in discrete action spaces. PPO is a policy gradient method where the agent learns a policy by optimizing a surrogate objective function [29]. The objective function for PPO is typically given as:

$$L^{CLIP}(\theta) = \hat{\mathbb{E}}_t \left[\min \left(r_t(\theta)\hat{A}_t, \text{clip}(r_t(\theta), 1-\epsilon, 1+\epsilon)\hat{A}_t \right) \right] \tag{2}$$

Where $r_t(\theta) = \frac{\pi_\theta(a_t|s_t)}{\pi_{\theta_{old}}(a_t|s_t)}$ is the probability ratio between the new and old policies. $\hat{A}_t$ is the advantage estimate at time t. ϵ is a hyperparameter controlling the degree of clipping.

In practical control tasks, considering obstacles in the environment is crucial. If the entire global environmental information is considered as the state space, the dimensionality of the state space would be very high, leading to increased training convergence time and significantly prolonged inference time. This would pose a significant challenge for the real-time output of the control policy. Therefore, we will use a path planning algorithm to pre-compute a series of trajectory points, ensuring that adjacent points in the trajectory do not intersect with obstacles. This simplifies the task by allowing the agent to complete a point-to-point task with minimal obstacles. By doing so, the difficulty of training is greatly reduced, enhancing the agent's control ability.

The path planning algorithm will output a sequence of points, and the agent will complete a single-point tracking task in the sequence until reaching the destination. The specific algorithm flow is shown in Figure 7.

In our project, the state space of the PPO agent is composed of the outputs from the visual recognition network and the path planning program. The output of the visual recognition network consists of the positions and tilt angles of the five detected points, which can be represented as

$$T = \begin{pmatrix} x_0 & y_0 & \phi_0 & \cdots \\ x_1 & y_1 & \phi_1 & \cdots \\ x_2 & y_2 & \phi_2 & \cdots \\ x_3 & y_3 & \phi_3 & \cdots \\ x_4 & y_4 & \phi_4 & \cdots \end{pmatrix} \tag{3}$$

where x_i, y_i, ϕ_i, $i \in \{0, 1, 2, 3, 4\}$ represents the coordinates and the orientation angle of the recognized points of the jellyfish. $\cdot$ implies the additional motion feature like the velocity and angular velocity.

The output of the path planning program consists of the XY coordinates of all points along the path, which can be represented as:

$$D = \begin{pmatrix} tx_0 & ty_0 \\ tx_1 & ty_1 \\ \vdots & \vdots \\ tx_{n-1} & ty_{n-1} \end{pmatrix} \tag{4}$$

where tx_i, ty_i, $i \in \{0, 1, \cdots, n-1\}$ represents the i-th target points in the target path. n reperesents the length of the target path.

The action space of the agent corresponds to the inputs of the control unit, where two-bit binary encoding controls the on/off status of the left and right electrodes of the jellyfish robot.

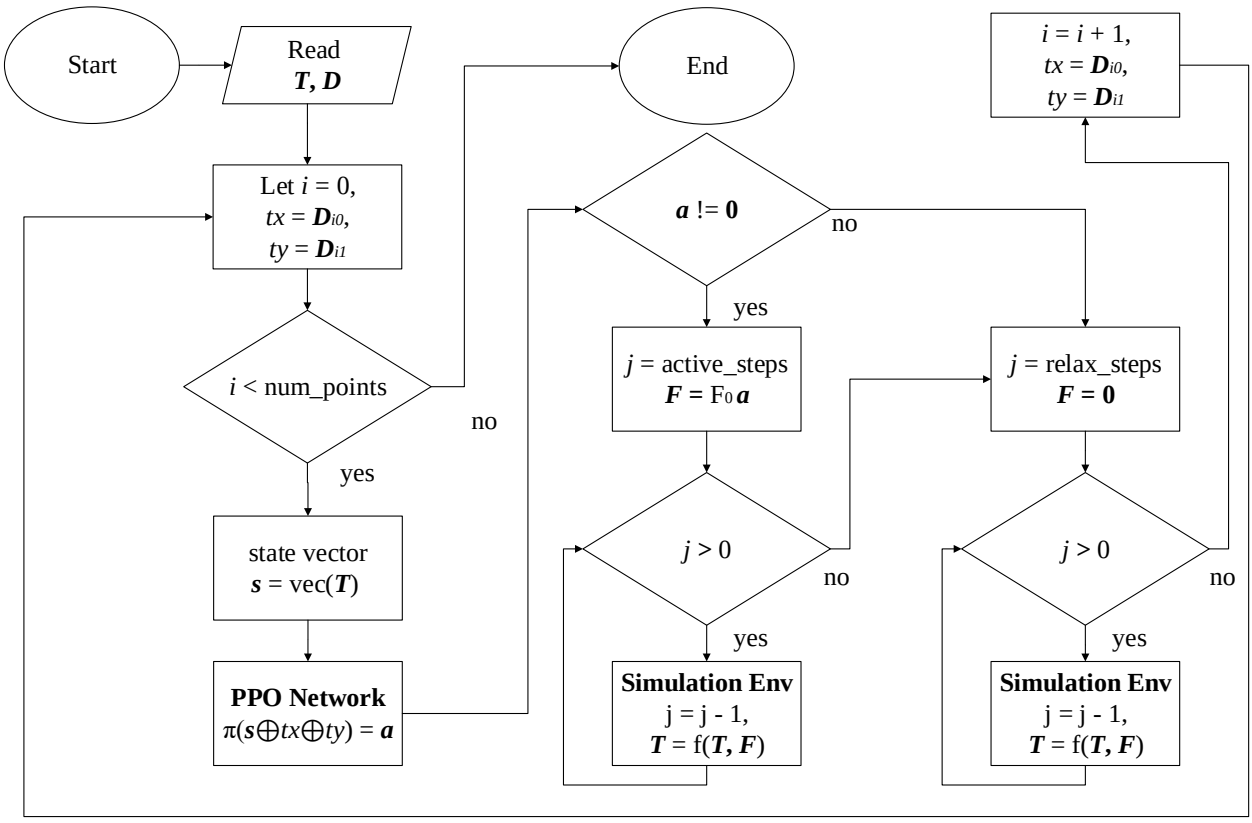

Figure 7: Flowchart of the RL control procedure. $\boldsymbol{T}$ is the matrix of position and attitude for each point on the jellyfish bot. $\boldsymbol{D}$ is the matrix of target points' x and y coordinates for each point on the planned path. $\boldsymbol{F}$ is the matrix of force given by the actuator. $\pi(\cdot)$ represents the mapping of PPO algorithm from observation space to action space. $f(\cdot)$ represents the mapping of the simulation environment from the last motion state and external force to the current motion state. s is the state vector of the PPO agents' input. a is a two dimensional binary vector of the PPO agents' output action, which is the direct command code to conduct the control unit's action. And it follows the same encoding rules in our control unit's design. $\text{vec}(\cdot)$ is the function that flatten the matrix. $\oplus$ is an operator that extend the vector with a scalar.

Table 3: Requirements and verification table for reinforcement learning control network.

Requirements	Verification
1. The RL control algorithm must accomplish single-point reaching tasks to any target circle (the final point should be within the distance of 2 times of the radius of the target circle) from any initial position and posture on its simulation platform. 2. The RL control algorithm must guide the simulated jellyfish robot along the planned path points provided by the path planning program. 3. The RL control algorithm must achieve a control speed of over 30 fps.	1. A. Validate that the control algorithm can reach the target circle from arbitrary start positions. B. Measure the distance from the endpoint to the target circle to ensure it falls within two radius $2R$. 2. A. Monitor the robot's motion to ensure it follows the predefined path. B. Validate that the path is effectively executed without hit the obstacles. 3. A. Benchmark the control speed across different scenarios to ensure it meets the 30 fps requirement. B. Implement logging to capture and analyze control speed over multiple trials.

2.3.4 Motion Planning Program

The Motion Planning Program is designed to help generate optimal paths for robotic movement, specifically in environments with obstacles. It allows users to define a starting point, a target endpoint, and the positions of circular obstacles in the space. Based on these inputs, the program computes a trajectory that the jellyfish robot can follow to reach its destination while avoiding obstacles.

The program works by dividing the environment into grids or triangles, abstracting the navigation space for pathfinding. It then applies shortest path algorithms or more advanced optimization methods to generate a sequence of waypoints that define the robot's trajectory. The resulting path is continuously updated and visualized in real-time, providing a clear representation of the robot's movement. This trajectory is then used as input for reinforcement learning (RL) agents, helping them learn to navigate through the environment and reach the target by avoiding obstacles. The program serves as both a planning tool and a visualization aid, ensuring that the jellyfish robot can safely and efficiently move towards its goal.

Table 4: Requirements and verification table for motion planning program.

Requirements	Verification
1. The path planning program must calculate a motion path with more than 5 points in $\geq$ 30 fps rate for the jellyfish based on target circle position, current position, and obstacles.	1. A. Count to ensure the path consists of more than five points. B. Validate that the calculated path does not intersect with any obstacles. C. Test the path planning algorithm against different scenarios and obstacles to ensure robustness and measure whether it meets the 30 fps planning speed.

2.4 Control Module

The control module transfer the data signal into the voltage signal.

2.4.1 Control Unit

The control unit is responsible for processing the two-bit binary information received from the infrared receiver and decoding it. It then converts the control code output by the RL algorithm into actual control outputs for the four-way relay hardware circuit. In a sense, the control unit acts as the lower-level machine in the RL control system. Specifically, the control unit uses the two-bit control code to manage the switching of the four relay circuits, which in turn controls the left and right electrodes of the jellyfish robot, ultimately controlling its movement.

The overall control logic is represented using a Moore state machine. A Moore state machine is a type of finite-state machine where the outputs depend only on the current state, not on the input. This makes it suitable for situations where the control logic is determined solely by the state of the system, rather than external inputs [30].

In the following context, our two kinds of Moore state machine will be introduced in detail. Building on this control logic, and taking into account the specific driving specifications for the jellyfish robot's electrodes, we also designed a PCB circuit to implement this control system effectively.

Moore State Machine

The state machine we initially developed is designed to control two electrodes based on input signals from an RC receiver, which is shown in Figure 8.

The machine takes three input bits:

- **First Bit (L)**: Indicates whether to activate the left electrode (1 = active, 0 = inactive).

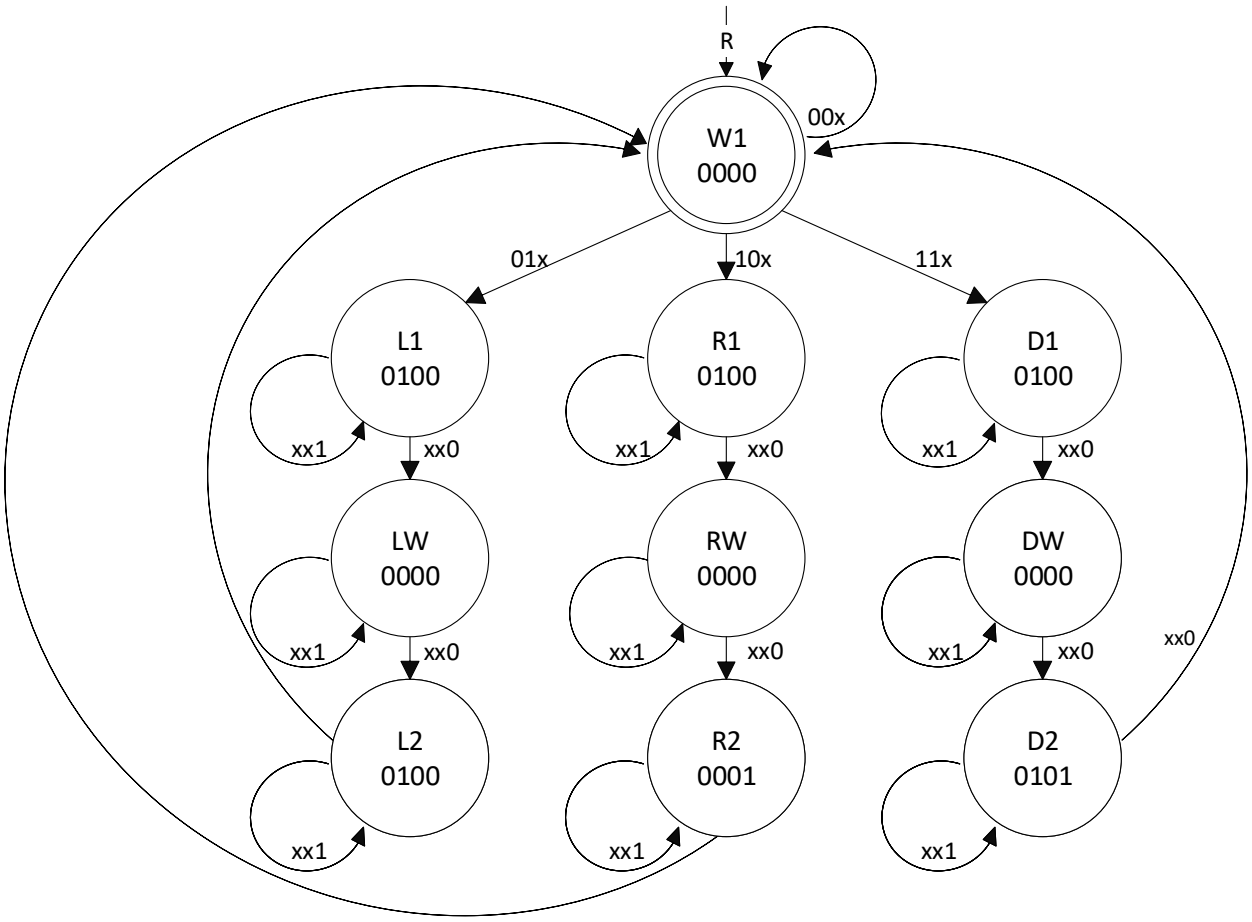

Figure 8: State diagram of our primary design. ”R” represents the Reset Signal, ”x” represents a ”don’t care” condition, meaning the state transition or output is the same for both 0 and 1 inputs. State name ”L*” relates to the drive of the left actuator, ”R*” relates to the right and ”D*” represents dual actuators are being driven.

- **Second Bit (R)**: Indicates whether to activate the right electrode (1 = active, 0 = inactive).
- **Third Bit (C)**: A hold signal that determines if the electrodes should continue operating (1 = continue, 0 = stop).

The output of the state machine is a single four-bit signal, which represents:

- **First Bit (L+)**: Indicates if the positive circuit of the left electrode is connected (1 = connected, 0 = not connected).
- **Second Bit (L-)**: Indicates if the negative circuit of the left electrode is connected (1 = connected, 0 = not connected).
- **Third Bit (R+)**: Indicates if the positive circuit of the right electrode is connected (1 = connected, 0 = not connected).
- **Fourth Bit (R-)**: Indicates if the negative circuit of the right electrode is connected (1 = connected, 0 = not connected).

The state transitions are based on the input signals, and the behavior of the machine can be represented in the state diagram provided, where different states correspond to different combinations of the input bits and control logic.

Table 5: Input signal meaning.

Bit Position	Signal	Meaning
1	L	Activate Left Electrode (1 = Yes, 0 = No)
2	R	Activate Right Electrode (1 = Yes, 0 = No)
3	C	Hold Signal (1 = Continue, 0 = Stop)

Table 6: Output signal meaning.

Bit Position	Signal	Meaning
1	L+	Left Electrode Positive Circuit
2	L-	Left Electrode Negative Circuit
3	R+	Right Electrode Positive Circuit
4	R-	Right Electrode Negative Circuit

This state machine has undergone an improvement to optimize the control of two electrodes based on the same three input signals from the RC receiver as in Figure 9.

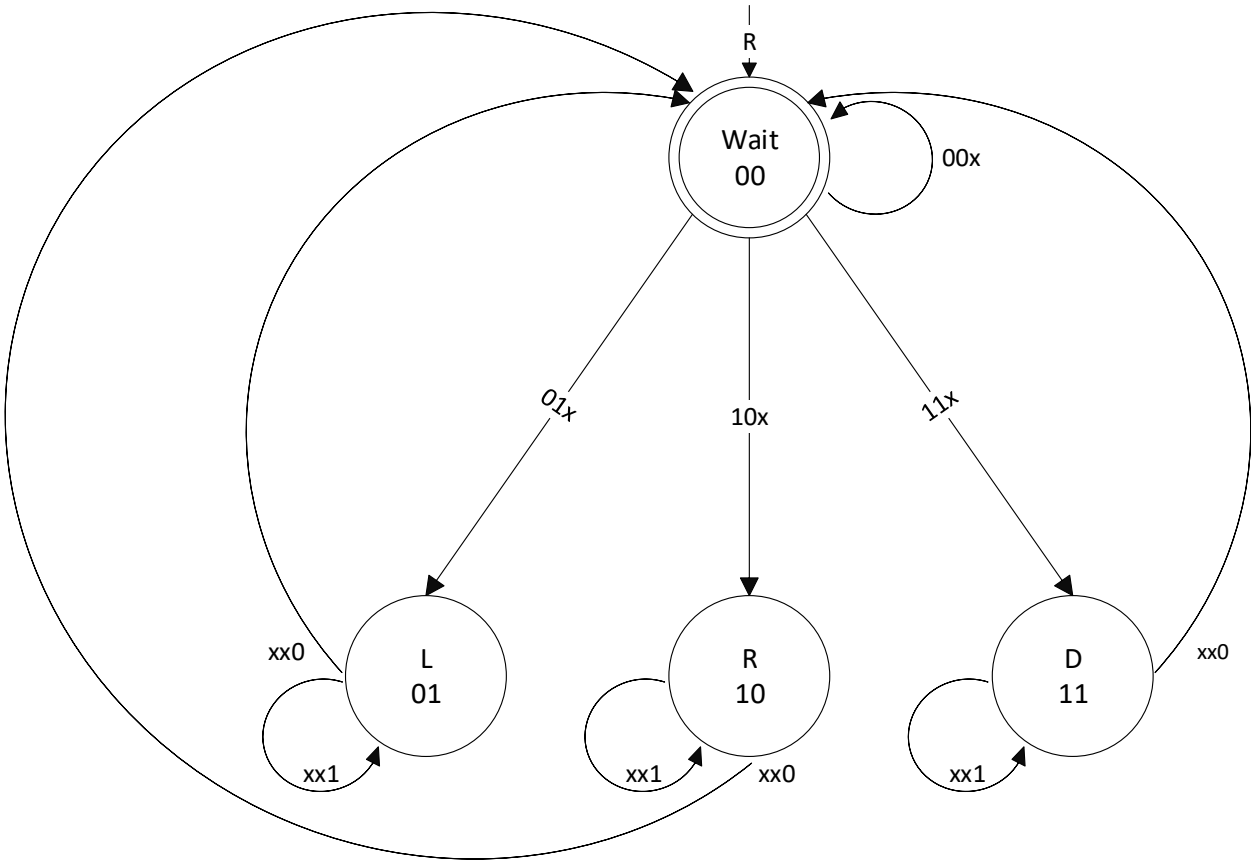

Figure 9: State diagram of our updated design with same meaning of ”R” and ”x”.

The machine still takes three input bits, with the same meaning as in Table 5. While the output of the state machine has been optimized to consist of a two-bit signal, which represents:

- **First Bit (O_L)**: Indicates if the left electrode should be activated based on the optimized strategy (1 = activated, 0 = not activated).
- **Second Bit (O_R)**: Indicates if the right electrode should be activated based on the optimized strategy (1 = activated, 0 = not activated).

Table 7: Output signal meaning.

Bit Position	Signal	Meaning
1	O_L	Activate Left Electrode (1 = Activated, 0 = Not Activated)
2	O_R	Activate Right Electrode (1 = Activated, 0 = Not Activated)

Here in Figure 10 is our circuit design, and Figure 11 is our PCB layout.

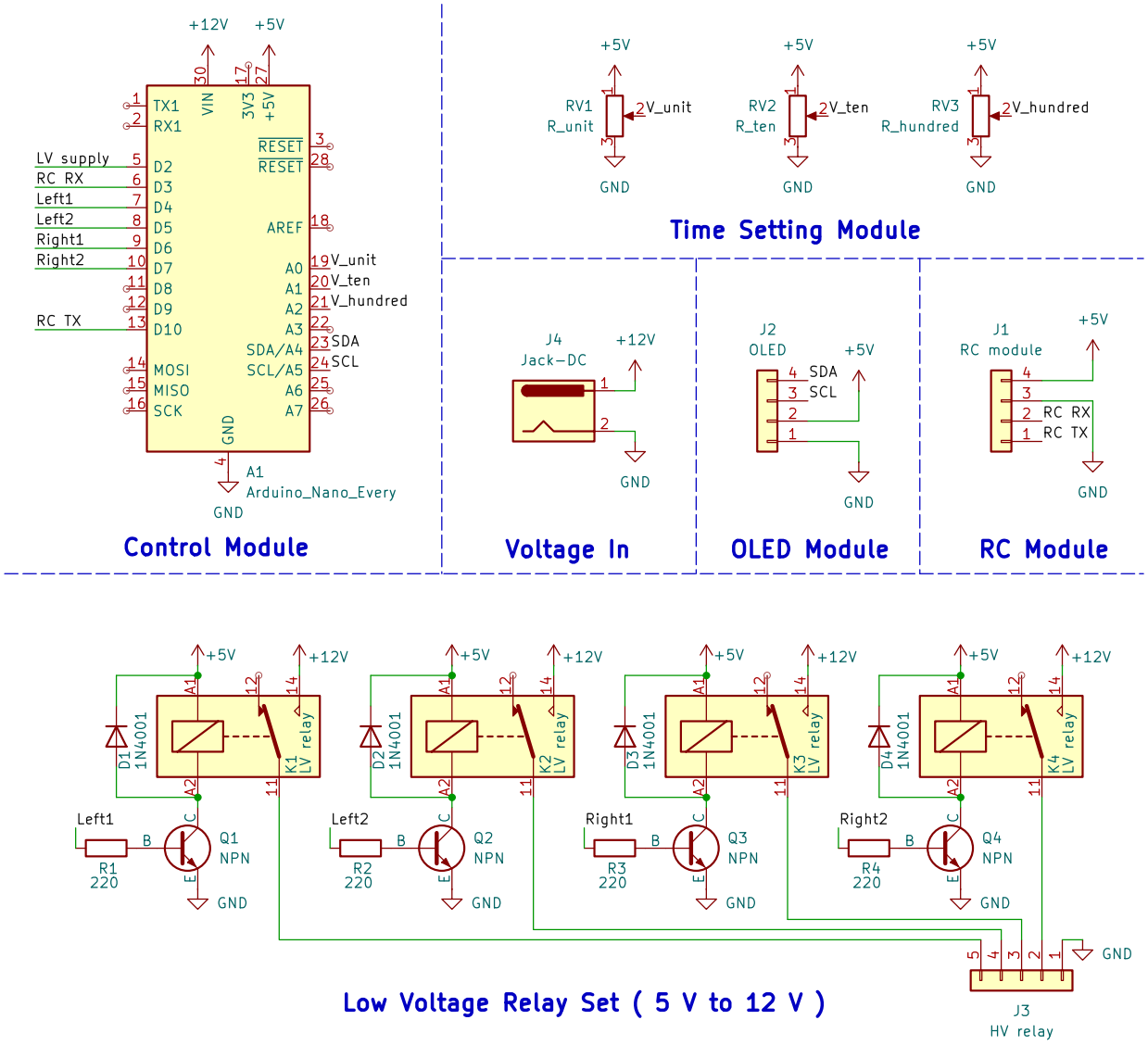

Figure 10: Circuit scheme of our control unit's hardware design.

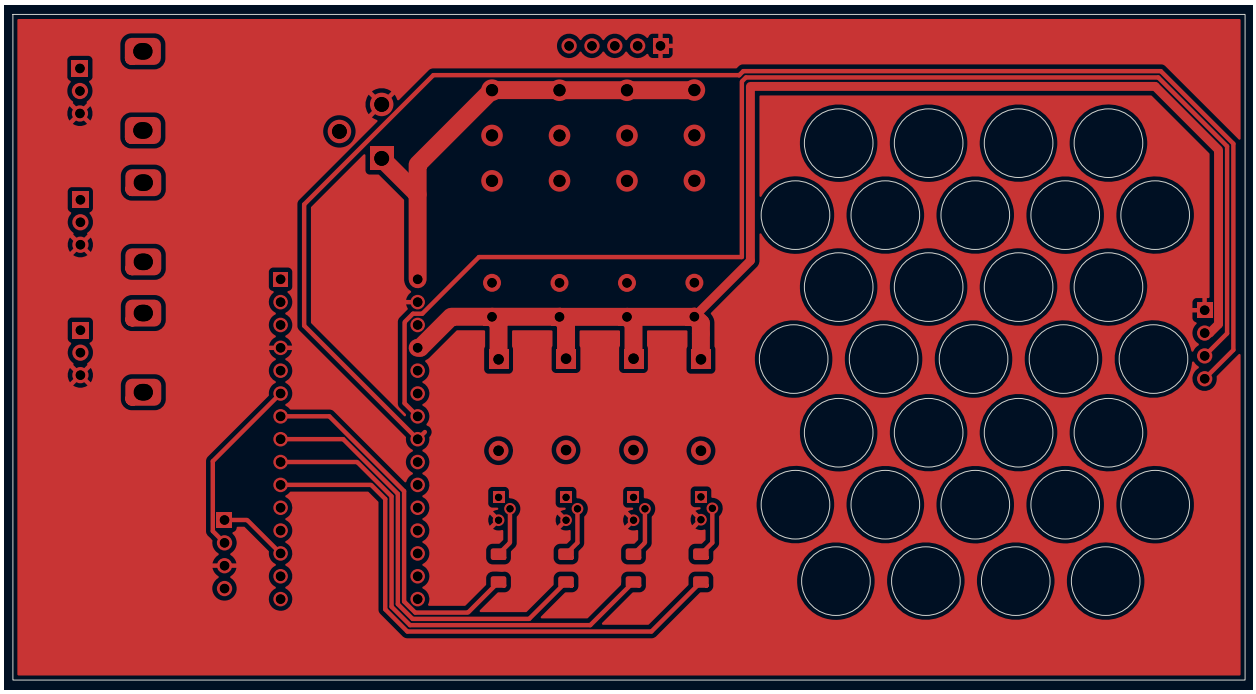

(a) Front copper layer only (F.Cu).

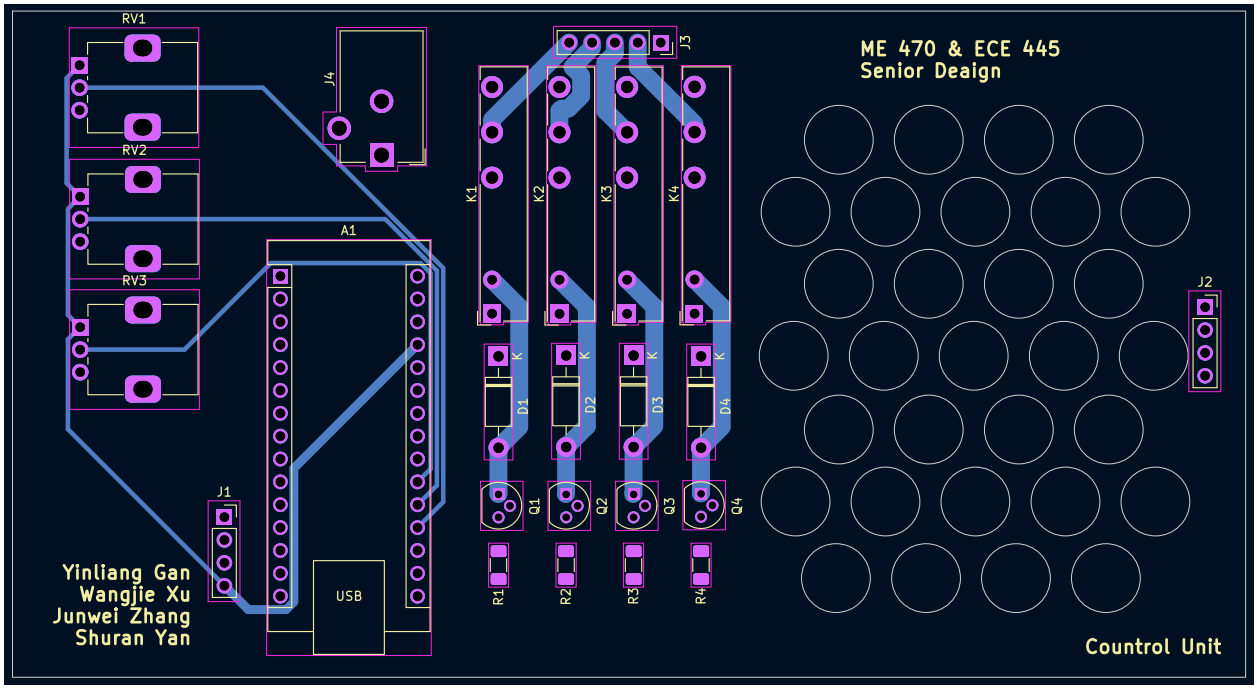

(b) All other PCB layers except F.Cu.

Figure 11: PCB layer visualization of the control unit. (a) Displays only the front copper layer (F.Cu), used for routing signal and power traces. (b) Shows all remaining PCB layers, including silkscreen, outline, vias, solder mask, and mechanical features.

Table 8: Requirements and verification table for control unit.

Requirements	Verification
1. The total control time for the jellyfish robot must be less than 150 ms. 2. The control unit must accurately respond to all commands and execute control outputs correctly.	1. A. Conduct latency testing by measuring the total time from input signal receipt to relay activation. B. Create a performance benchmark to ensure that the control time consistently meets the 150 ms requirement. 2. A. Perform unit testing to verify that each command (namely, 00, 01, 10, 11) results in the correct relay activation or deactivation. B. Document all test results to confirm that the control unit responds accurately across different scenarios.

2.4.2 HV Relay Set

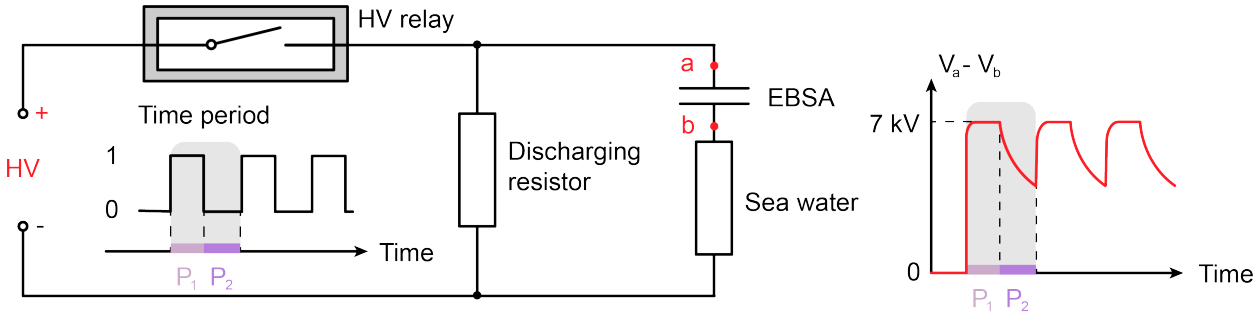

Figure 12: Single-relay direct drive control of an EBSA. Here a control cycle contains two phases, the first one is the charging phase and the second one is discharging phase.

Initially, we employed the simplest HV driving method, using only a single HV relay to control the EBSA, as illustrated in Figure 12. In this configuration, the discharge resistor is directly connected between the HV positive and negative terminals during conduction. As a result, the resistor must withstand the full driving voltage, requiring a HV-rated component. We therefore selected a 100 MΩ resistor with sufficient voltage tolerance. However, we observed that during repeated actuation of the EBSA, the initial cycle consistently exhibited significantly stronger deformation compared to subsequent cycles. This prompted a further investigation into the cause of this phenomenon.

As a first step, we examined the electro-physical properties of the non-electrical components in the system. Since the EBSA is composed of two parallel electrodes separated by dielectric oil and a dielectric elastomer layer (VHB 4905), it can be approximately modeled as a multilayer capacitor. According to the datasheets, the relative permittivity of

VHB 4905 is 3.21 [31], [32], while that of the silicone oil (PMX200 0.65 cSt) is 2.2 [33], [34]. Based on our measurements, the thicknesses of the VHB and the oil layers during actuation were 0.2 mm and 0.05 mm respectively, and the electrode area was 5 cm × 5 cm. Using the standard capacitance formula for multilayer dielectrics:

$$\frac{1}{C_{\text{total}}} = \frac{d_{\text{VHB}}}{\varepsilon_0 \varepsilon_{\text{VHB}} A} + \frac{d_{\text{oil}}}{\varepsilon_0 \varepsilon_{\text{oil}} A}, \tag{5}$$

we calculated the total capacitance of the EBSA to be approximately 0.2603 nF.

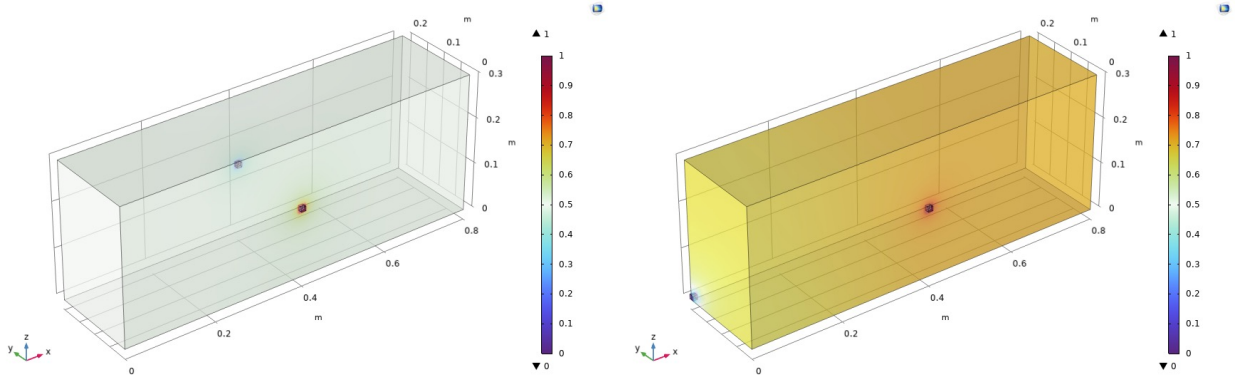

(a) Voltage distribution (corner)

(b) Voltage distribution (center)

Figure 13: Voltage distribution in seawater. The small copper cubes represent electrodes. The front cube corresponds to the electrode immersed in seawater during the 2D-BJR demonstration, while the rear cube represents the 2D-BJR unit itself. In the finite-conductivity domain (FCD) simulation, we set the front cube to 1 V and the back cube to 0 V. By performing surface integral of current density, we obtained total currents of 0.033781 A and 0.057464 A for (a) and (b), respectively. This corresponds to equivalent resistances of 29.6 Ω and 17.4 Ω. Therefore, we can reasonably assume that the effective resistance between the 2D-BJR and the input terminal of the HV amplifier through seawater is always less than 29.6 Ω.

Since most jellyfish naturally inhabit marine environments [35], we used seawater (tap water with added salt) as the experimental medium. In our system, the seawater serves as the conductive pathway between the actuator and the HV source. Given that the electrical conductivity of seawater is significantly lower than that of copper, we considered it necessary to quantify its electrical resistance. According to literature, the conductivity of seawater at 20 °C is approximately 4.8 S/m. Based on this value, we performed finite-element simulations using COMSOL and found that the resistance of the seawater in our configuration is less than 29.6 Ω, as shown in Figure 13.

During the charging process, as Figure 12 P_1, the discharge resistor is directly connected in parallel with the power supply, and thus does not affect the capacitor charging behavior. As a result, the original circuit can be simplified into a standard DC RC charging circuit, in which the EBSA is modeled as a capacitor C, and the series resistor R_{sea} accounts for the sea water resistance of the circuit.

The voltage $V_C(t)$ across the capacitor during charging follows the classical exponential

relationship:

$$V_C(t) = V_0 \left(1 - e^{-\frac{t}{R_{\text{sea}}C}}\right), \tag{6}$$

where:

- V_0 is the applied voltage,
- R_{sea} is the effective series resistance,
- C is the total capacitance of the EBSA,
- t is the time since the voltage was applied.

To calculate the time required for the capacitor voltage to reach 99% of the applied voltage, we solve:

$$V_C(t) = V_0 \left(1 - e^{-t/R_{\text{sea}}C}\right) = 0.99V_0.$$

Given $R_{\text{sea}} < 29.6\ \Omega$ and $C = 0.2603$ nF, the time required to charge the capacitor to 99% of the input voltage satisfies:

$$t = 4.605 \cdot R_{\text{sea}}C < 4.605 \cdot 29.6\ \Omega \cdot 0.2603 \times 10^{-9}\ \text{F} \approx 35.4\ \text{ns}.$$

Therefore, the charging time to 99% of full voltage, which can be regard as full voltage, is less than 35.4 ns. Thus, we can neglect the charging time of EBSAs.

During the discharge process, as Figure 12 P_2, the total resistance consists of the discharge resistor and the seawater resistance in series, resulting in an effective resistance of:

$$R_{\text{total}} = R_{\text{discharge}} + R_{\text{sea}} = 100\ \text{M}\Omega + 29.6\ \Omega = 1.000000296 \times 10^8\ \Omega.$$

The voltage across the capacitor during discharge decays exponentially as:

$$V_C(t) = V_0 \cdot e^{-t/R_{\text{total}}C}. \tag{7}$$

To determine the time required for the voltage to drop to 50% of its initial value, we solve:

$$0.5 \cdot V_0 = V_0 \cdot e^{-t/R_{\text{total}}C} \Rightarrow t = R_{\text{total}}C \cdot \ln(2) \approx 0.693 \cdot R_{\text{total}}C.$$

Given $C = 0.2603$ nF $= 2.603 \times 10^{-10}$ F, we obtain:

$$t = 0.693 \cdot 1.000000296 \times 10^8 \cdot 2.603 \times 10^{-10} \approx 18.06\ \text{ms}.$$

Therefore, the time required for the EBSA to discharge to 50% of its initial voltage through the combined resistance is approximately 18.06 ms. This time is considerably long relative to the actuation cycle. To achieve continuous movement in the robot, we are likely to set the duration of P_2 to less than 1 second. Consequently, the experimental result shows that: the first actuation cycle produces significantly greater movement compared to subsequent cycles.

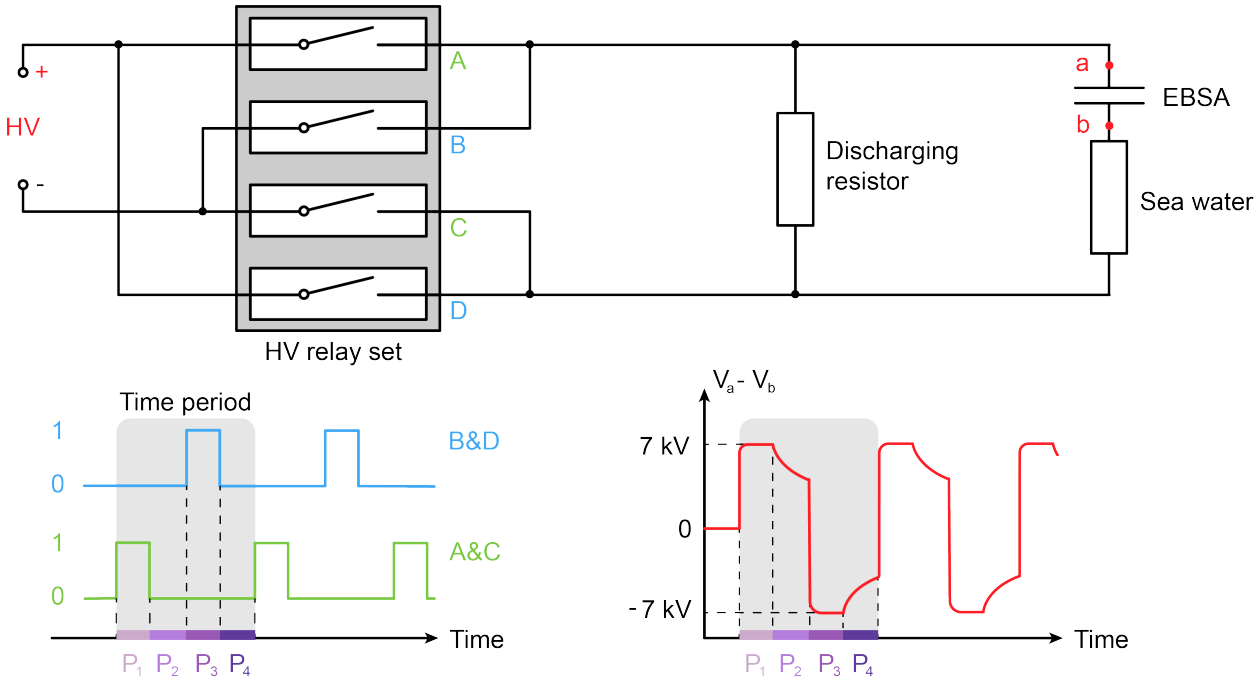

Figure 14: Four-relay inverted polarity control strategy for EBSA. Here a control cycle contains four phases, the first one is the charging phase, the second one is discharging phase, the third one is reverse charging phase, and the last phase is another discharging phase.

Therefore, it was natural for us to consider applying a reverse voltage to eliminate the residual charges that had accumulated due to incomplete discharge, as shown in Figure 14. Although the discharge process in this configuration still suffers from a relatively slow decay rate, the reverse voltage effectively performs a discharge-then-recharge sequence during each cycle. This approach successfully improves the consistency of the robot's actuation performance across multiple cycles. As a result, we finalized this strategy and completed the design schematics before April 4th.

Figure 15 shows the circuit diagram of this relay integration scheme, while Figure 16 presents its corresponding PCB layout.

However, this driving method also presents three critical drawbacks that limit its practical application.

First, in this configuration, the HV terminal is directly connected to the seawater tank. This poses a significant safety risk, as it greatly increases the possibility of leakage current through the conductive medium. Given the HV involved, any unintended conduction through the water could be hazardous to both the system and the operator.

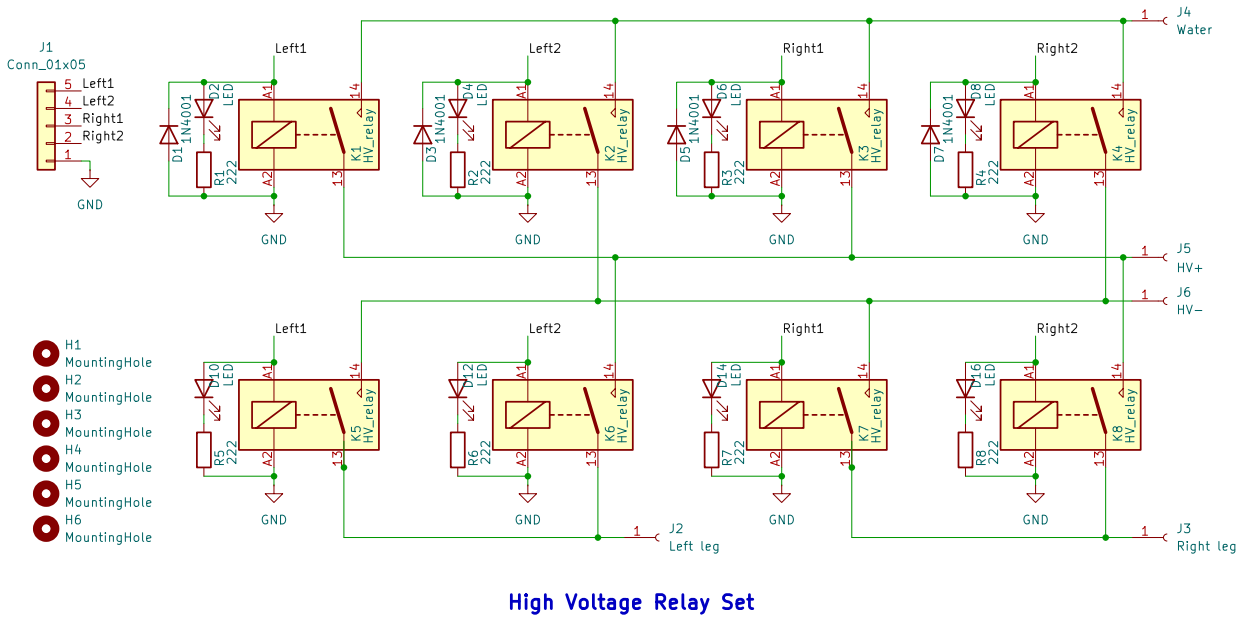

Figure 15: Schematic diagram of the HV relay set circuit.

Second, the actuation method inherently requires two opposite-direction actuations to complete a full operating cycle. Without this bidirectional motion, the control logic would become highly complex and difficult to implement in a real-time control system. However, if we treat two actuations as a single control unit, the effective control resolution is halved. This severely degrades the accuracy of our trajectory-following algorithm and limits the system's responsiveness to external inputs or path adjustments.

Finally, the implementation cost of this approach is notably high. Each actuation unit requires four HV relays, which considerably increases both the hardware complexity and the overall budget. For systems requiring multiple actuators, this cost scales rapidly and becomes a major obstacle to scalability and deployment.

To overcome the aforementioned limitations, we returned to a charge–discharge control strategy. However, unlike our initial implementation, we decoupled the charging and discharging loops by designing a new circuit, as shown in Figure 17. In this configuration, Relay A is driven by a pulsed control signal, while Relay B is always driven with the inverse of A's signal. During **Phase 1**, Relay A is closed and Relay B is open. The HV amplifier charges the EBSA through a low-resistance path, similar to previous methods. Using Equation 2.4.2, given the capacitance $C = 0.2603$ nF and a charging resistance $R_{\text{sea}} < 29.7\ \Omega$, and 99% charging completes in:

$$t_{\text{charge}} < 4.605 \cdot R_{\text{sea}} C \approx 35.4 \text{ ns}.$$

During **Phase 2**, Relay A opens and Relay B closes. The EBSA is then connected in an RC discharge loop through seawater and a discharge resistor. The total resistance is:

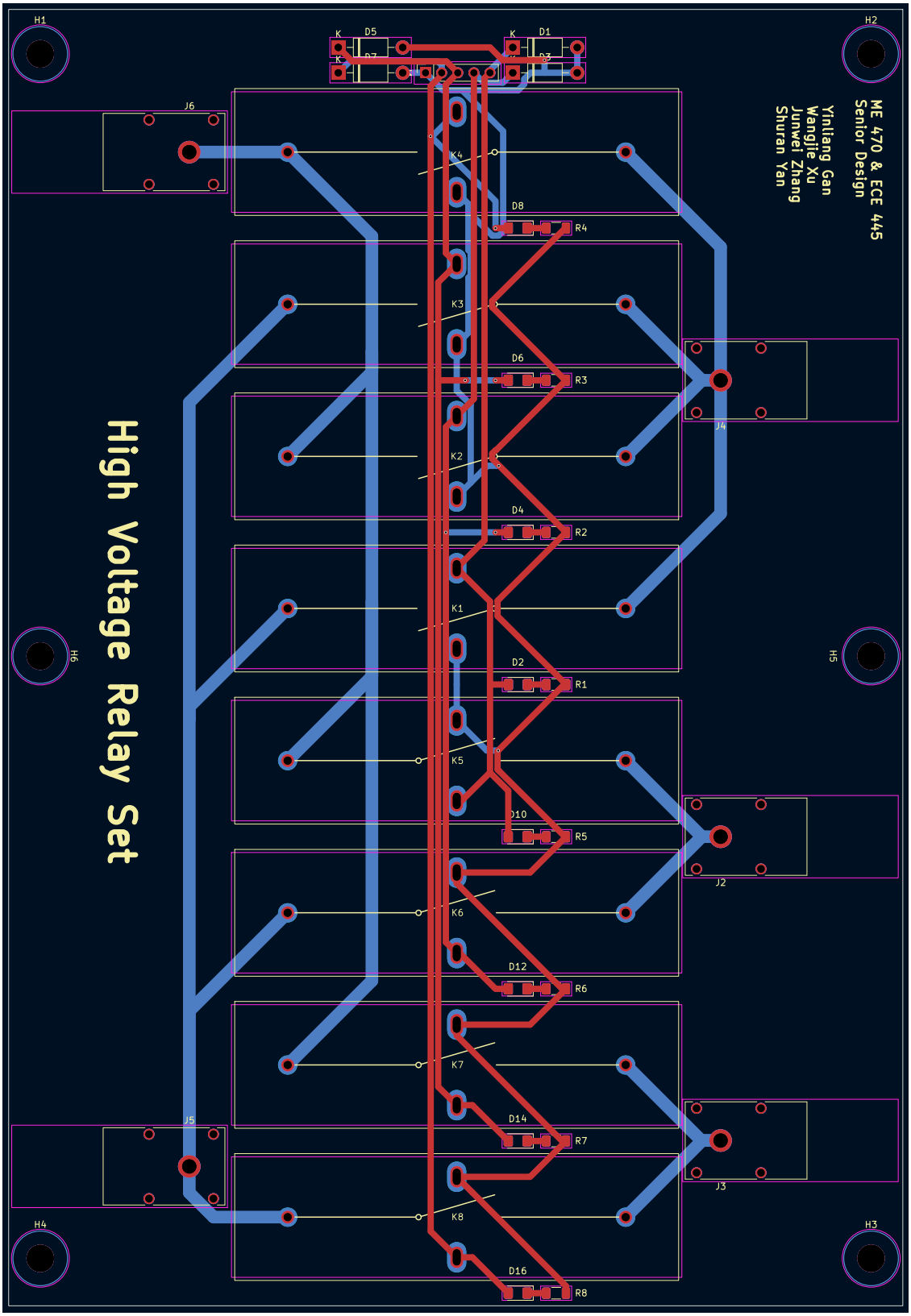

Figure 16: Corresponding PCB layout of HV relay set circuit.

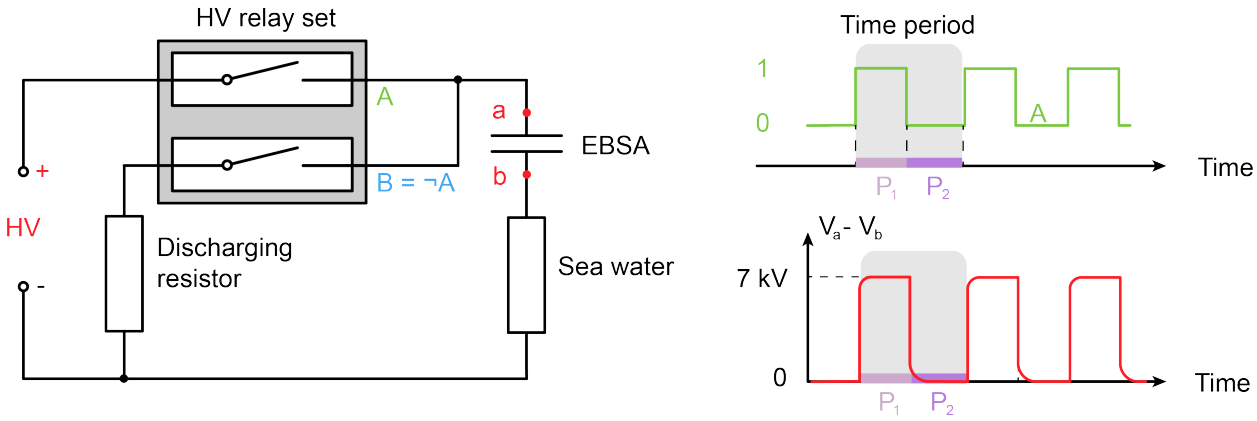

Figure 17: Two-relay controlled discharge strategy for safe and reversible EBSA actuation. A control cycle consists of two phases: a charging phase and a discharging phase. The discharge resistor used in this configuration has a resistance of 1000 Ω, which is acceptable because it is not connected during the charging phase and therefore is not exposed to the full supply voltage. Moreover, the current during the discharge phase is extremely small, such that even if the instantaneous power briefly exceeds the resistor's rated power, it does not lead to damage or reliability issues.

$$R_{\text{total}} = R_{\text{sea}} + R_{\text{discharge}} < 29.6\ \Omega + 1000\ \Omega = 1029.6\ \Omega$$

Using the exponential voltage decay equation as Equation 7, we compute the time required for the voltage to drop to 1% of its initial value:

$$t < 4.605 \cdot R\text{total}C = 4.605 \cdot 1029.6 \cdot 2.603 \times 10^{-10} \approx 1.23\ \mu\text{s}.$$

This discharge time is sufficiently short to be negligible in the context of the actuation cycle. Therefore, the redesigned two-relay circuit ensures that the EBSA is fully discharged between cycles, enabling consistent and high-performance actuation behavior.

Based on the above analysis and comparative evaluation, we ultimately adopted the optimized version of the HV relay set design. This configuration effectively separates the charging and discharging pathways using two relays, ensuring both safety and consistent performance of the EBSA during cyclic operation. To meet project deadlines, the circuit design was completed under a tight schedule on April 5th. The finalized circuit schematic is shown in Figure 18, and the corresponding PCB layout is provided in Figure 19.

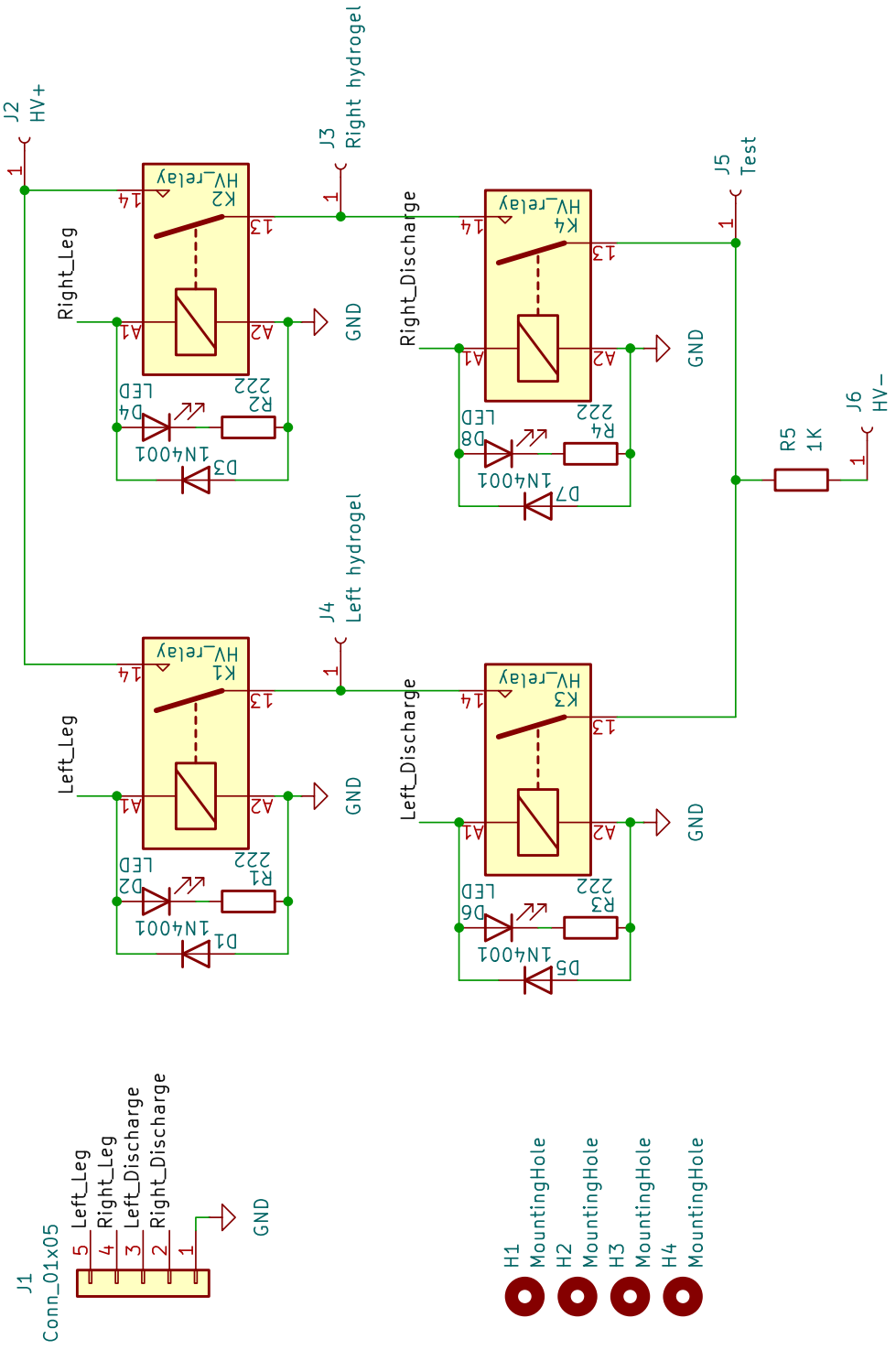

Figure 18: Final schematic diagram of the HV relay set circuit, illustrating the independent control of the charging and discharging paths via two coordinated relays.

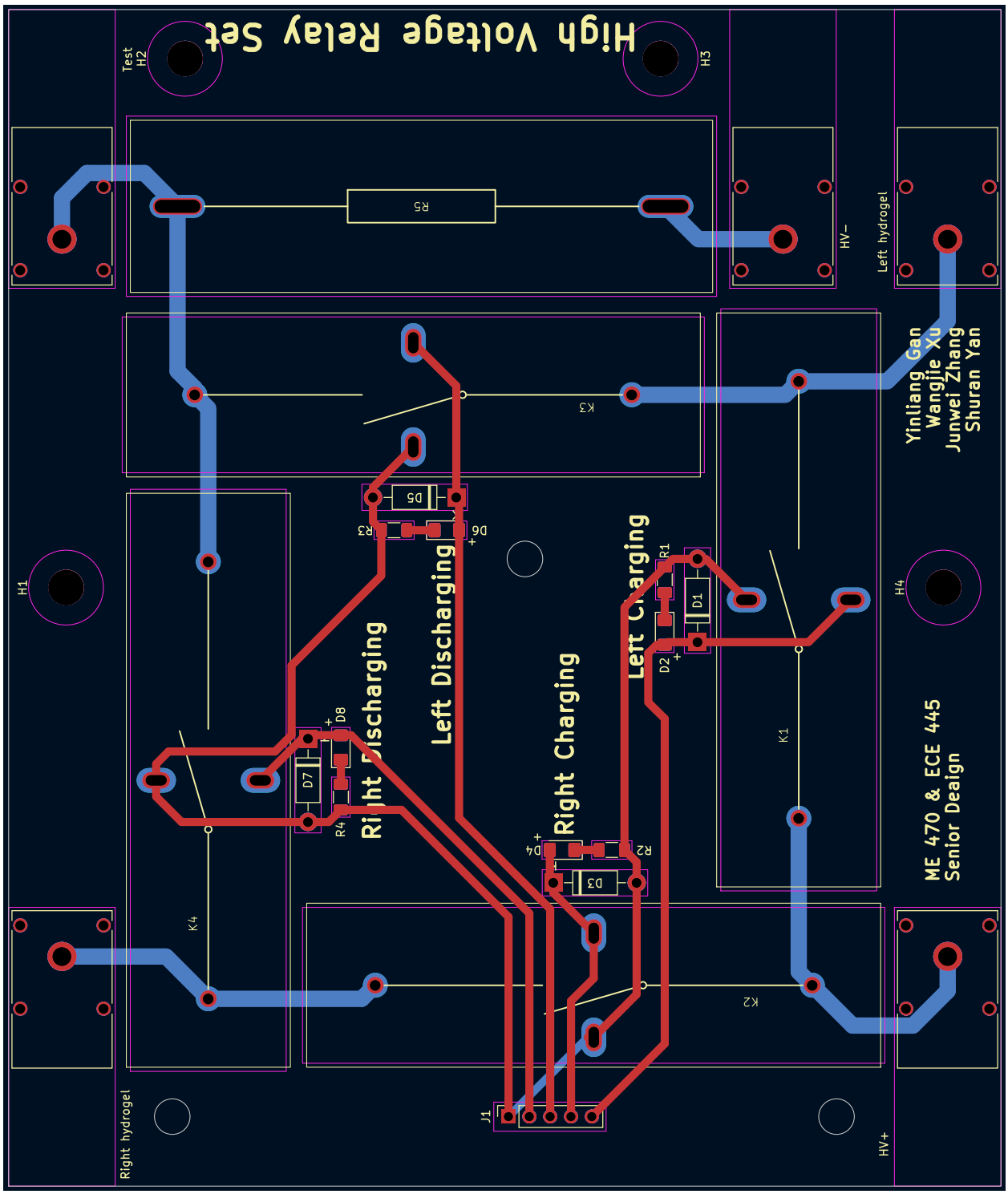

Figure 19: Corresponding PCB layout of the final HV relay control system, implementing the dual-relay strategy in a compact and robust form for reliable experimental use.

Table 9: Requirements and verification table for HV relay set.

Requirements	Verification
1. The relay circuit must ensure complete charge and discharge of the EBSA within each control cycle. 2. The switching of relays must be safe and should avoid exposing seawater to HV terminals. 3. The control circuit must remain cost-effective and scalable for multiple EBSA units.	1. A. Measure the time for charging (to 99%) and discharging (to 1%) of the EBSA using oscilloscope monitoring. B. Confirm charging time is below 1 ms and discharging time is below 1 ms because we need to let the actuator response as soon as possible. 2. A. Inspect circuit layout to verify that the HV output is never directly connected to seawater. B. Test multiple actuation cycles to ensure no abnormal leakage or performance degradation occurs. 3. A. Verify that the entire circuit operates using only two relays per actuator unit. B. Compare component costs and evaluate PCB size reduction compared to the four-relay design.

2.5 Actuation Module

The actuation module makes 2D-BJR able to move.

2.5.1 HV Amplifier

The **HV Amplifier** is used to amplify low-voltage signals to the HV required by certain system components, in our project, the actuation module. For this project, we will be using the **MR HV amplifier** provided by laboratory. This amplifier can output a voltage of up to ±10 kV with a maximum power of 20 W, suitable for HV power supply and testing.

Technical Specifications:

- Output Voltage: ±10 kV
- Output Power: 20 W
- Input Signal: 0-10 Vdc or ±10 Vdc (adjustable)
- Output Signal: ±10 kV
- Current Limit: ±10 Vdc, maximum current is 2 mA

Table 10: Requirements and verification table for HV amplifier.

Requirements	Verification
1. The amplifier must provide a sufficient voltage gain to meet system requirements. The output signal must remain clean, without significant noise or distortion.	1. A. Connect the input signal and verify the output voltage using a multimeter or oscilloscope. B. Check the signal quality to ensure that amplification does not introduce significant noise or distortion.

2.5.2 HV Relay Set

As detailed in Section 2.4.2, the implementation here follows the exact same design and logic, and is thus omitted for redundancy.

2.5.3 2D-BJR: Hydrogel Electrode Layer

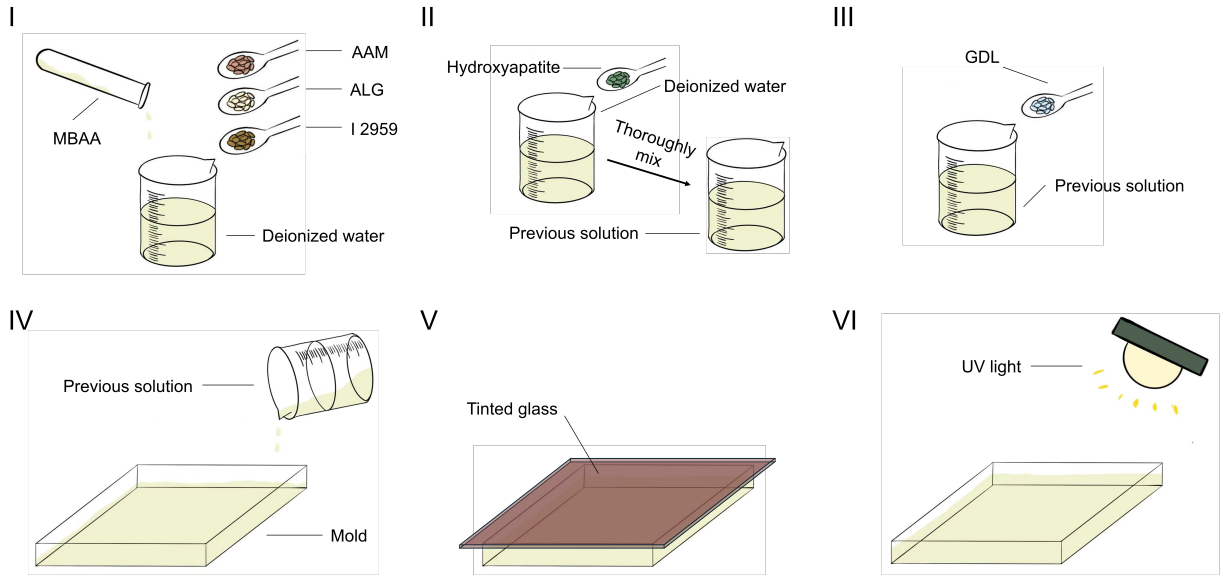

Figure 20: Synthesis process of hydrogel testing samples.

Preparation: Figure 20 illustrates the preparation process of the hydrogel. In the first step, 19.31 g of Acrylamide (AAM), 2.41 g of Sodium Alginate (ALG), 0.14 g of 2-Hydroxy-4'-(2-hydroxyethoxy)-2-methylpropiophenone (I 2959), and 0.69 mL of N, N'-Methylenebisacrylamide (MMBA) solution (0.1 mol/L in deionized water) are dissolved in 100 mL of deionized water. In the second step, 0.08 g of Hydroxyapatite ($Ca_{10}(PO_4)_6(OH)_2$) is dissolved in 4.55 g of deionized water, and this solution is thoroughly mixed into the precursor solution prepared in the first step. Next, 0.46 g of D-(+)-Gluconic acid δ-lactone (GDL)

is added to the mixture and mixed thoroughly. The solution is then deaerated, and the resulting mixture is poured into a glass mold. A tinted glass lip is used to cover the mold, and it is stored at 20 °C for 12 hours to allow the hydrogel to undergo its first crosslinking. After 12 hours, the mold is exposed to UV light (365 nm) for 30 minutes to complete the second crosslinking process.

Test: A series of tests were performed to assess the mechanical strength, electrical conductivity, and water absorption characteristics of the hydrogel samples.

- (a) After the hydrogel is solidified, remove it from the mold and use the stretch sample cutting knife to make a hydrogel stretch sample. Use caliper to measure the thickness and width of the stretch sample. After that, use the universal testing machine to stretch the sample at a specific rate and record the force versus time data. Use these data to get a stress–strain curve, thus we can get the elastic modulus and yield strength of the hydrogel sample. Use the universal testing machine to stretch and compress the sample continuously, record the stress-strain property after every 100 cycles. Calculate the fatigue life and fatigue strength of the sample.
- (b) Use the rectangular cutting knife to cut a rectangular sample. Use the caliper to test the length, width, and thickness of the sample. Apply a uniform layer of conductive carbon paste to two sides of the hydrogel sample. Use the power supply and current voltage measure machine to test the IV (current versus voltage) curve of the sample. Calculate the resistance and the conductivity from these data.
- (c) Use the rectangular cutting knife to cut another rectangular sample. Dry the hydrogel samples at 60 °C for 24 h and weigh it. Then immers it in deionized water for 2 hours. Weigh it after removing it from the water with filter paper. Calculate the water absorption ratio from these two weights.
- (d) Change the portion of AAM and ALG to make different types of hydrogel samples. Test the stretch property and conductivity again. By comparison, select the best recipe which has high elastic modulus, high fatigue life, and high conductivity to be the final material of the electrode.

Table 11: Requirements and verification table for 2D-BJR (hydrogel electrode layer).

Requirements	Verification
1. The hydrogel must withstand repeated mechanical deformation without rupture. It should exhibit a high elastic modulus, good tensile strength, and excellent fatigue resistance under cyclic loading. 2. The hydrogel must provide stable and sufficient conductivity to function as an electrode, enabling efficient charge transfer during actuation and sensing. 3. As a water-rich material, the hydrogel must retain adequate water content over time to maintain its mechanical and electrical performance.	1. Tensile tests were performed using standardized stretch samples cut from solidified hydrogel. The stress–strain curves were obtained from force–time data collected by a universal testing machine, allowing the calculation of elastic modulus and yield strength. Fatigue life and strength were determined by subjecting samples to repeated stretching and compression cycles. 2. Samples with defined dimensions were coated with conductive carbon paste on both sides. A current-voltage (IV) curve was measured using a source meter, from which the resistance and electrical conductivity were calculated. 3. Dried hydrogel samples were weighed before and after immersion in deionized water. The water absorption ratio was determined based on the change in mass, reflecting the material's water retention capability.

2.5.4 2D-BJR: Main Actuation Structure

Preparation: Figure 21 illustrates the fabrication process of a linear DE-HASEL actuator, which serves as the core component of the 2D-BJR. First, two rectangular VHB films were cut and set aside. A piece of release paper was then trimmed into a rectangle—slightly longer but narrower than the VHB films—and sandwiched between the two VHB layers. The regions of the VHB not covering the release paper were pressed together and fully bonded. Next, silicone oil was injected into the release-paper-covered region using a syringe and manually spread evenly along the inner surface of the VHB pouch. The release paper was then carefully removed. Air bubbles were gently pushed out from the pouch, and a new piece of VHB was applied to seal the opening, completing the fabrication of the linear DE-HASEL actuator. To fabricate the 2D-BJR structure, two hydrogel substrates with pre-defined shapes were prepared. Unstretched VHB was first laminated onto the surface of one hydrogel. The pre-stretched linear DE-HASEL actuator was then bonded to the opposite side of the hydrogel (where no VHB was attached). Upon releasing the prestretch, the internal stress caused the structure to morph into a jellyfish-like configu-

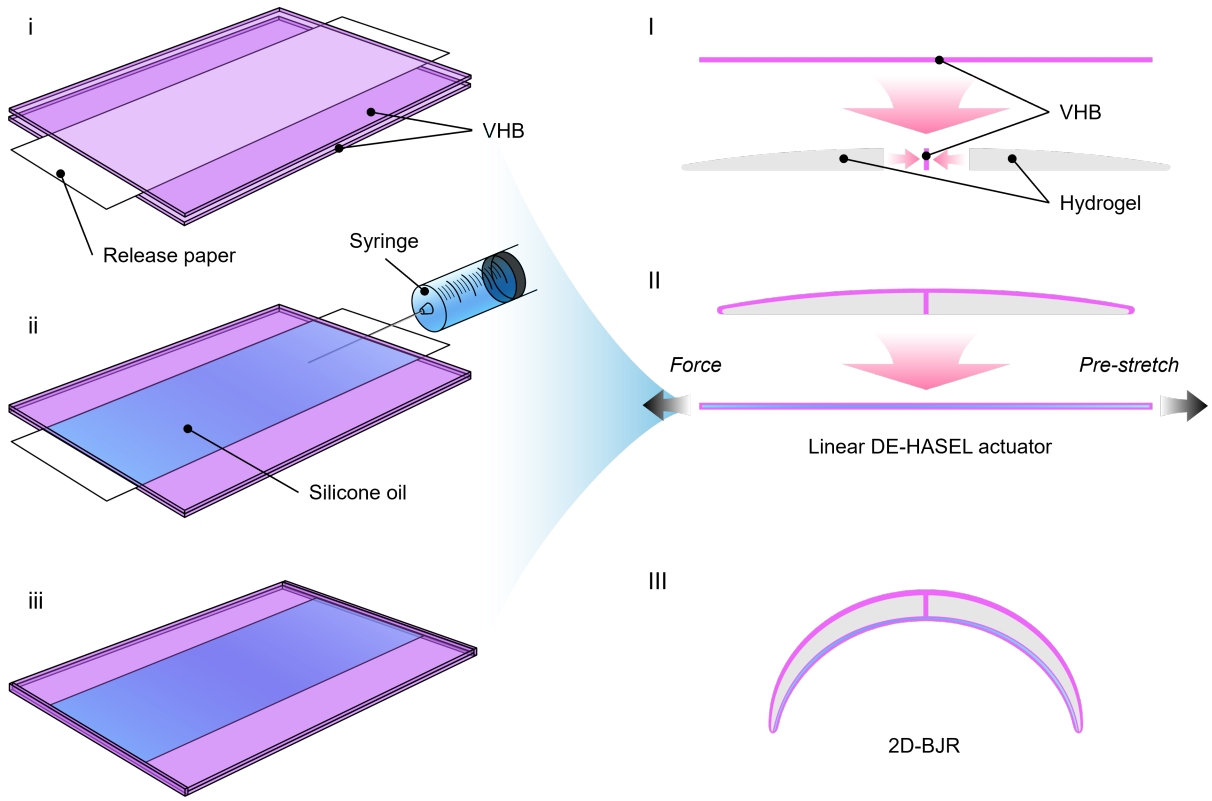

Figure 21: Manufacture process of 2D-BJR.

ration, thus forming the final 2D-BJR actuator.

Test: Figure 22 illustrates the prestretching test conducted on the linear DE-HASEL actuator. First, carbon paste electrodes were applied to both sides of the fabricated actuator. Carbon paste was selected because, being a liquid electrode, it does not impose additional mechanical stress during stretching, thereby minimizing systematic error. Additionally, its inherent dark color facilitates the visual observation of deformation in the electrode region. Next, both ends of the actuator were clamped between two acrylic plates and secured using mechanical grips. A lead screw mechanism was rotated to gradually stretch the actuator. The deformation of the electrode region after prestretching was then measured. Subsequently, actuation tests under different applied voltages were performed. For each voltage level, the generated force and corresponding deformation were recorded. By analyzing the results across multiple voltage and strain conditions, the optimal prestretching ratio for the actuator was determined.

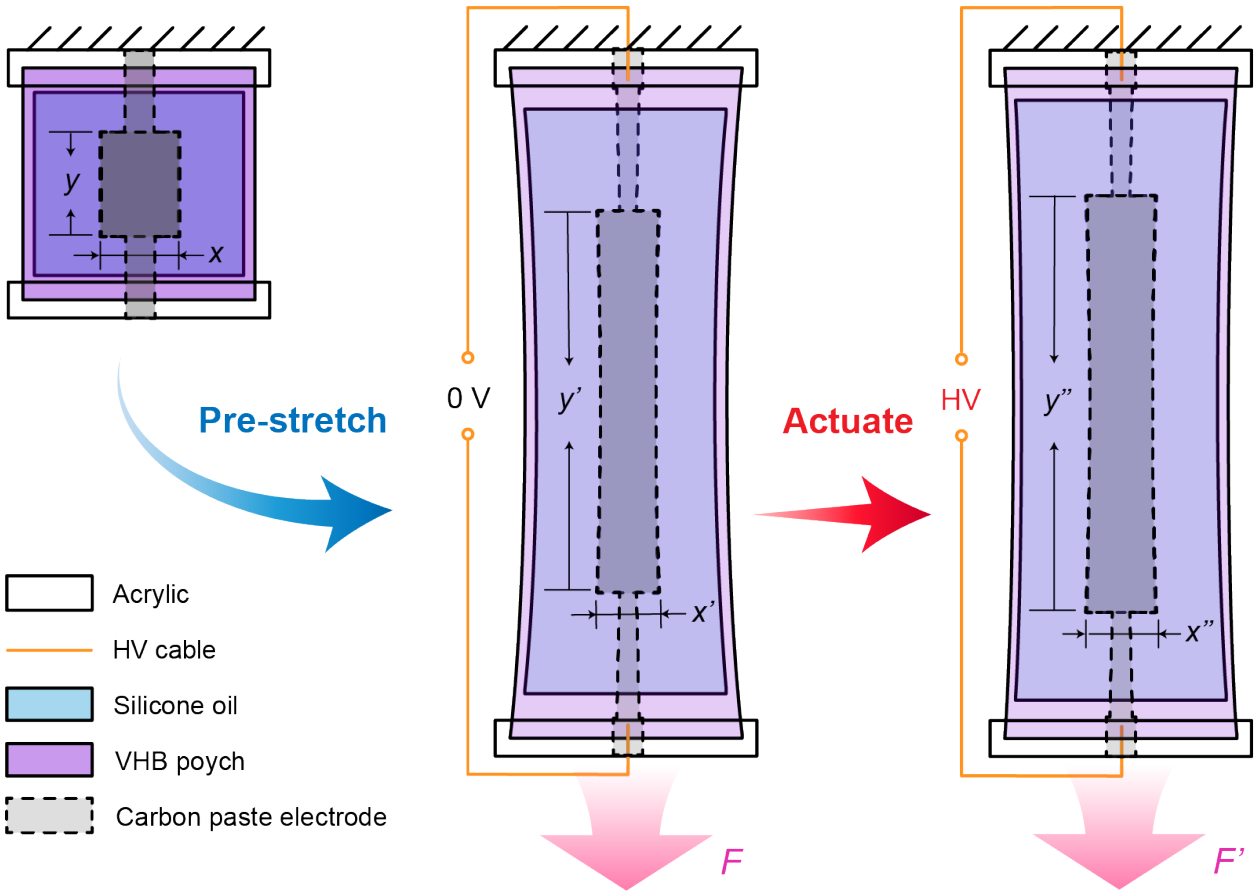

Figure 22: Pre-stretch experiment of linear DE-HASEL actuator.

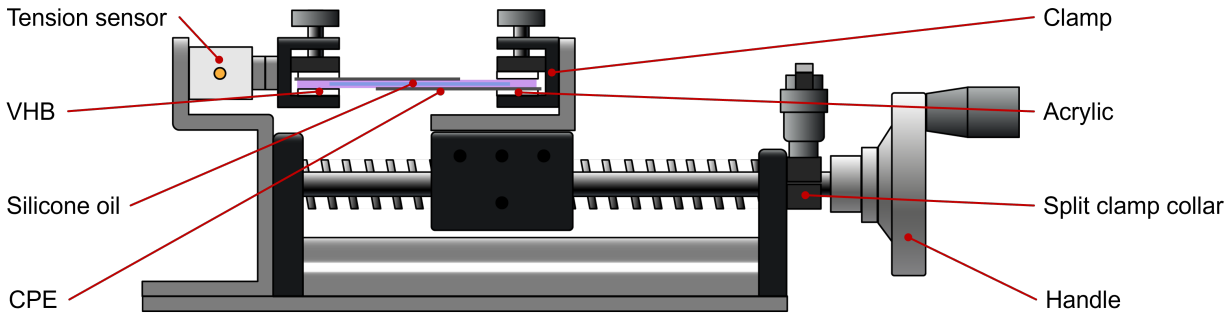

Figure 23: Pre-stretch experiment setup.

Table 12: Requirements and verification table for 2D-BJR (main actuation structure).

Requirements	Verification
1. The VHB films must form a well-sealed pouch that securely contains the silicone oil without leakage or air entrapment, ensuring consistent electrohydraulic actuation. 2. The actuator must be prestretched to a level that maximizes its actuation efficiency, defined by the generated force and deformation under applied voltage, without compromising mechanical stability or lifespan. 3. The actuator must be firmly bonded to the hydrogel interface such that post-stretch release induces the expected 3D morphing into a jellyfish-like configuration, forming the final 2D-BJR structure.	1. The fabrication steps (Figure 21) were followed by visual inspection to confirm that the VHB pouch was properly sealed, air bubbles were removed, and the silicone oil was evenly distributed. Any visible defects such as leakage, swelling, or trapped bubbles led to sample rejection. 2. A. A mechanical setup using acrylic plates and a lead screw (Figure 23) was used to gradually stretch the actuator. Deformation was measured after each prestretching level, and actuation tests were conducted at different voltages to record force and deformation output. B. Multiple tests were performed with varying stretch ratios. The output force and displacement at each voltage were analyzed to determine the stretch level that offered the highest actuation performance while maintaining mechanical stability. 3. After bonding the prestretched actuator to the hydrogel and releasing the tension, the final 2D-BJR was formed. The characteristic dome-like morphology was confirmed visually, verifying that internal residual stress induced the expected jellyfish-inspired 3D shape.

2.6 Peripherals

2.6.1 IR Signal Module

The **IR Signal Module** consists of three main components:

IR Signal Sender: The IR signal sender transmits infrared signals provided by the computing node, enabling communication with the control unit module. It is responsible for encoding and sending the relevant control signals to the IR receiver.

IR Signal Receiver: The IR signal receiver captures the infrared signals transmitted by the sender. It decodes the signals and relays the received information to the control unit for further processing.

TTL to USB Cable: The TTL to USB cable (CH340G model with indicator LED) interfaces the IR signal module with the computing node. It facilitates communication between the IR signal receiver and the laptop via the USB port, converting TTL signals into USB-compatible data.

Table 13: Requirements and verification table for IR signal module.

Requirements	Verification
1. The IR signal module must support both signal transmission and reception. 2. The TTL to USB cable must function correctly for data exchange between the IR receiver and the computing node. 3. The signal transmission and reception must occur reliably with delays less than 100 ms.	1. A. Connect the IR signal sender and receiver to the TTL to USB cable, and connect the cable to the laptop. B. Verify that both the sender and receiver can communicate with the computing node by checking if signals are successfully received and transmitted. 2. A. Connect the TTL to USB cable to the laptop and launch the system testing tool. B. Ensure that the IR receiver is recognized and correctly communicates with the laptop by verifying successful data transfer. 3. A. Record the process of signal transmission. Be sure to record the indicator lights of the transmitters and receivers on both sides. B. Calculate the number of frames between the two lights starting to flash in the video file, and divide by the frame rate to obtain the number of seconds. Check whethe it's less than 0.1s.

2.6.2 Camera

The **Camera** is responsible for capturing video input, which will be processed by the computing node for object detection and recognition. It must provide real-time, high-quality video data to ensure accurate analysis.

Table 14: Requirements and verification table for camera.

Requirements	Verification
1. The camera must capture high-quality video with a minimum frame rate of 30 FPS. The camera should have a sufficient resolution to allow object detection algorithms to function accurately.	1. A. Connect the camera to the computing node and ensure that the video feed is visible and stable. B. Verify that the captured video is being processed by the object detection system without significant lag or loss of frames.

2.6.3 Square Wave Generator

The **Signal Generator** is used to generate the necessary signals for controlling various components in the system. We will be using the **AFG1022** model, a square wave signal generator. This device can generate square waves at different frequencies and amplitudes to produce the required driving signals for the experiment.

Table 15: Requirements and verification table for square wave generator.

Requirements	Verification
1. The square wave generator must be capable of generating square waves at configurable frequencies. The output waveform must be stable and free from significant distortion.	1. A. Connect the generator to the system and test the output frequency. B. Use an oscilloscope to verify the stability and shape of the square wave signal.

2.6.4 Glass Water Tank

The **Glass Water Tank** is a transparent enclosure used for housing and testing the jellyfish model. It must provide an appropriate environment for the jellyfish and allow clear visibility for video monitoring.

Table 16: Requirements and verification table for glass water tank.

Requirements	Verification
1. The tank must be transparent and large enough to accommodate the jellyfish model comfortably. The tank must have the ability to contain water without leaks.	1. A. Check the transparency of the glass and the capacity of the tank for the jellyfish bot. B. Test the tank for leaks by filling it with water and checking for any signs of leakage.

2.7 Tolerance Analysis

Critical Functionality: The most critical requirement of our jellyfish-inspired robot is that it must be able to track and follow a desired trajectory using discrete, count-based actuation commands, despite sensing delays, actuator uncertainty, and control signal latency. The robot's ability to do so depends on the accuracy of the control loop in both time and amplitude.

Involved Subsystems and Parameter Tolerances:

- *Actuation Granularity:* The robot's propulsion is based on discrete action counts $n_t \in \{0, 1, 2, ...\}$, each contributing a fixed displacement $\Delta x = 2.5 \text{ mm}$. Due to mechanical backlash and water resistance, the actual displacement per pulse varies within $\pm 10\%$, i.e., $\Delta x \in [2.25, 2.75] \text{ mm}$.
- *Control Delay:* The system has a known action execution delay of $\tau = 2$ time steps. However, due to communication latency and task scheduling jitter, the actual delay may vary by ± 1 step.
- *Sensor Precision:* The onboard position sensor has a resolution of 1 mm and an accuracy of $\pm 2 \text{ mm}$. Noise is assumed to be bounded and zero-mean.
- *Control Quantization:* The RL controller outputs discrete counts n_t, but the policy network outputs continuous values which are rounded to integers. Rounding introduces a quantization error of at most ± 0.5 count.

Mathematical Model with Tolerance:

The state update equation under delay and discrete control is:

$$x_{t+1} = x_t + n_{t-\tau} \cdot \Delta x \tag{8}$$

The tracking error at time t is:

$$e_t = r_t - x_t \tag{9}$$

The error update becomes:

$$\Delta e_{t+1} = (r_{t+1} - r_t) - n_{t-\tau} \cdot \Delta x \tag{10}$$

Now, considering all tolerances, the worst-case error change is:

$$\Delta e_{t+1}^{\text{worst}} = \pm\delta_r - (n_{t-\tau} \pm 0.5)(\Delta x \pm 10\%)$$

where $\delta_r = \max |r_{t+1} - r_t|$ is the maximum slope in the reference trajectory.

Oscillation Tolerance Criterion:

To avoid sustained oscillation, the error should not repeatedly cross zero. From our earlier derivation:

$$|e_t| < n_{t-\tau} \cdot \Delta x \quad \Rightarrow \quad \text{Oscillation risk} \tag{11}$$

Given the maximum possible error due to actuation quantization and delay jitter, we compute the critical error threshold:

$$|e_t|_{\text{critical}} = (n_t + 0.5) \cdot 1.1 \cdot \Delta x \approx (n_t + 0.5) \cdot 2.75 \text{ mm}$$

For instance, when $n_t = 2$, the critical window is about ± 6.875 mm. If the system remains within this band under worst-case parameter variation, oscillation is likely.

Simulation-Based Tolerance Testing:

We conducted a simulation sweep over the following parameter ranges:

- $\Delta x \in [2.25, 2.75]$ mm
- $\tau \in \{1, 2, 3\}$
- Sensor noise $\sim \mathcal{U}(-2, +2)$ mm

The RL controller was trained under nominal parameters and tested under worst-case combinations. The tracking error remained bounded with peak values less than 15 mm, which is within our system's acceptable deviation threshold of 20 mm.

Figure 24: Error vs jump count.

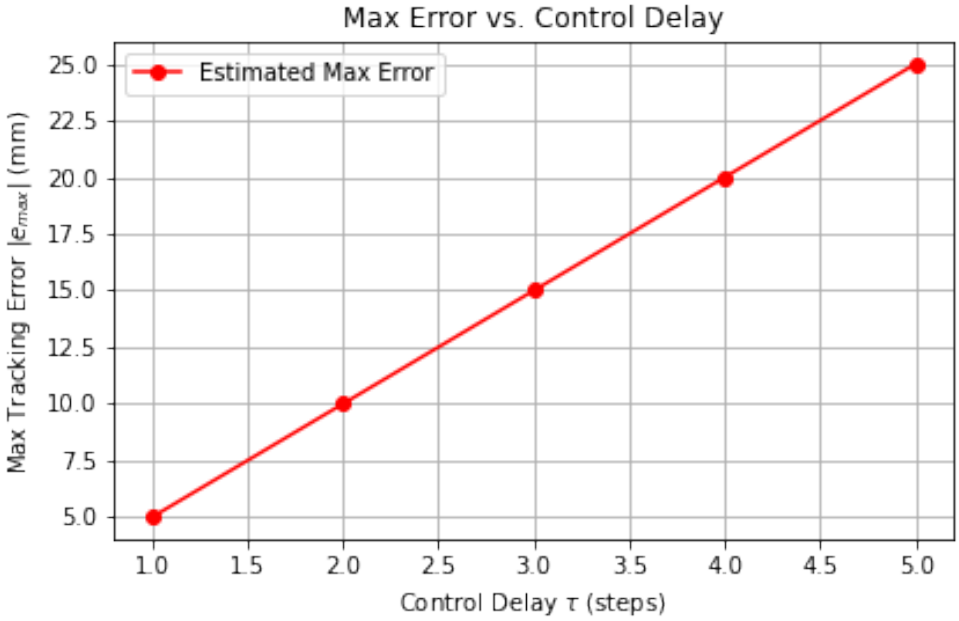

Figure 25: Max error vs control delay.

3 Cost and Schedule

3.1 Cost Analysis

Table 17: Cost table from Mar. 1st to Apr. 7th

Time	Item	Description	Quantity	Price
3/23	Silicone oil	0.65 cSt, 1 L	1	39
3/23	VHB	3M 4095, 100 mm*3 m*1 mm	1	108
3/23	VHB	4M 4095, 100 mm*3 m*0.5 mm	1	138
3/23	Hydrogel	58*87 mm	48	102.4
3/27	Hydrogel	80*80 mm	40	87.2
3/27	Glass tank	80*40*20 mm	1	206
3/27	Camera	12 MP, USB-A	1	227
3/27	Pigment	12 color	1	30
3/28	Ball screw linear guide	100 mm	1	100
3/28	Notebook	A5	5	39.5
3/28	High voltage relay & PCB	CRSTHV-20KV-A, 12 V, PCB footprint	4+1	876
3/29	RC module	infrared signal transmission and reception module, 2.54 mm, straight pins	2	38
3/29	USB to TTL cable	USB to serial downloader cable, CH340G with indicator light	1	9.74
3/30	SMD resistor	1206, 220R	100	7
3/30	Pin socket	2.54 mm, 1*15P, straight	10	2.5
3/30	DC power jack	5.5*2.5 mm	15	23.7
3/30	Arduino Nano Every	ABX00028, ATMega4809	1	119.99
3/30	Transistor	BTA201-800ER	20	14
3/30	Relay	FTR-LYCA005Y	6	82
3/30	Potentiometer	ALPS RK09 B10K	10	50

Continued on next page

Table 17 Continued from previous page

Time	Item	Description	Quantity	Price
3/30	Pin header & socket	2.54 mm, 1*40P, round	3+3	16.2
3/30	Dupont cable	1*5P, 100 mm, single-ended header with tinned ends	2	3.66
3/30	OLED module	IIC, 2.42 inch	1	40
3/30	Pin socket	2.54 mm, 1*4P & 1*5P, straight	4+2	15.5
3/30	DC power adapter	12 V, 1 A	1	13.5
3/30	Rectifier diode	1N4001, 1 A, 50 V	50	50
3/30	SMD LED	1206, red	100	2.5
3/30	SMD resistor	1206, 222	100	3.9
3/30	Banana jack	SMD, 4 mm	5	22.25
3/31	Optical plate holder	BHOMT0207	2	220
3/31	Screw & nut	5*12 mm (*80), 5*6 mm (*150), 6*9mm (*60), M5 (*50)	1	39.93
3/31	CNC machining	custom-made	3	400
3/31	Cable	banana plug to alligator clip	5	32.5
3/31	Dupont cable	1*5P, 100 mm, double-ended header	2	4.06
3/31	PCB	custom-made, control unit	5	80.62
4/1	High voltage relay	CRSTHV-20KV-A, 12 V, PCB footprint	4	777
4/1	PCB	custom-made, HV relay set	5	125
4/3	CNC machining	custom-made	4	500
4/3	Screw	4*5 mm (*200)	1	12.7
4/3	Tension sensor	0 to 200 N	1	195
4/3	Analog transmitter	12 V (input), 0-5 V (output)	1	158
4/3	Screw	3*12 mm (*200)	1	14
4/3	Data acquisition card	DAM-3158A, 8P, 2^{16}, 10 Hz	1	279

Continued on next page

Table 17 Continued from previous page

Time	Item	Description	Quantity	Price
4/3	DC power adapter	24 V, 2 A	1	60
4/3	Protocol converter	USB-A to RS485, 1.5 m	1	139
4/3	DC power jack	5.5*2.5 mm, DC005Z	9	4.2
4/4	PCB	custom-made, control unit	5	170.9
4/4	PCB	custom-made, HV relay set 2	5	189.79
4/4	Nylon hex standoff	M4, 1 set	1	23
4/4	HV resistor	30 W, 1000 R	4	28
4/4	Stretch sample cutting knife	GB/T 1040.3-2006 1B	1	79.3
4/4	Quartz glass square tank	inside 200*100*10 mm, thinkness 3 mm, lid 200*100*3 mm	1	180
4/4	wood box	30*20*10.5 cm	1	32.8
4/4	UV Curing box	365 nm, 240 w, 230*170*155 mm	1	936.32

The content presented in Table 17 does not represent the actual cost of developing a 2D-BJR system. The table includes not only the cost of the actuators and materials used in the project but also the expenses for various testing equipment. Since developing a new actuator system requires thorough characterization of its performance—such as testing its response times, force outputs, deformation capabilities, and durability—the cost of instruments used in these tests is factored into the overall expenditure. This includes specialized equipment such as testing rigs, sensors, and measurement tools necessary for evaluating the actuators under various conditions.

Additionally, as this project is research-focused rather than product-oriented, the costs associated with prototyping, iterative testing, and troubleshooting are considerably higher than those that would be incurred when the robotic system is eventually implemented in real-world applications. In practical use, once the system is refined and optimized for a specific task, the overall cost would likely decrease due to reduced testing requirements and the ability to source materials more efficiently at scale.

Therefore, while the figures in the cost table provide a comprehensive overview of the research and development expenses, they do not reflect the true operational cost of the system when it is deployed in a real-world environment, where economies of scale and simplified manufacturing processes would significantly lower the cost of production.

3.2 Schedule

Table 18: Detailed Graduation Project Timeline (April 14 – May 23, 2025)

Week	Date (2025)	Detailed Tasks	Member(s)
1	Apr 14–16	Prepare initial hydrogel samples	Junwei Zhang
	Apr 17–20	Preliminary mechanical and water absorption tests	Junwei Zhang
	Apr 14–18	Fabricate initial DE-HASEL actuators	Yinliang Gan
	Apr 19–20	Initial optimization of actuator fabrication	Yinliang Gan
	Apr 14–20	Capture ∼700 images of 3D-printed jellyfish	Shuran Yan
	Apr 14–20	Refine jellyfish simulation model and bug fixing	Wangjie Xu
2	Apr 21–24	Detailed mechanical tests (elastic modulus, fatigue life)	Junwei Zhang
	Apr 25–27	Electrical conductivity tests	Junwei Zhang
	Apr 21–27	DE-HASEL actuator prestretch experiments	Yinliang Gan
	Apr 21–27	Train preliminary detection and ReID algorithms	Shuran Yan
	Apr 21–27	Visualize data and conduct initial RL training	Wangjie Xu
3	Apr 28–30	Finalize optimal hydrogel formula and verify properties	Junwei Zhang
	May 1–4	Fabricate hydrogel electrodes	Junwei Zhang
	Apr 28–May 2	Assemble actuator with hydrogel electrodes	Yinliang Gan
	May 3–4	Initial jellyfish robot structural assembly	Yinliang Gan
	Apr 28–May 4	Refine dataset and algorithms; start angle calculation	Shuran Yan
	Apr 28–May 4	RL optimization and begin path planning scripts	Wangjie Xu

Continued on next page

Table 18 Continued from previous page

Week	Date (2025)	Detailed Tasks	Member(s)
4	May 5–8	Waterproof sealing	Yinliang Gan
	May 9–11	Finalize robot assembly	Yinliang Gan
	May 5–11	Complete angle calculation algorithm	Shuran Yan
	May 5–11	RL tracking for arbitrary targets and debug path planning	Wangjie Xu
5	May 12–15	Produce final datasets integrating real robot movements	Yinliang Gan, Shuran Yan
	May 16–18	Verify jellyfish robot line-following performance	Yinliang Gan, Shuran Yan
	May 12–18	Achieve sequential target RL tracking; start FSI simulations	Wangjie Xu
6	May 19–23	Integrate visual recognition, RL control, and physical actuation; validate infrared communication; conduct complete system testing	All Members

4 Discussion of Ethics and Safety

4.1 Ethical Considerations

4.1.1 Adherence to IEEE Code of Ethics

This project aligns with the IEEE Code of Ethics by:

- **Ensuring public safety and ethical research practices:** The soft underwater robot is designed to operate autonomously in underwater environments without harming underwater life or damaging the ecosystem. All testing is first conducted in controlled environments.
- **Protecting data privacy and security:** The vision-based sensing system collects underwater images for navigation and target detection purposes only. All data handling follows ethical data collection and storage protocols.
- **Maintaining integrity and accuracy:** The robot must operate with high reliability to prevent navigation errors that could result in unintended environmental interactions. To ensure accurate perception and behavior, we will conduct repeated measurements and validation under controlled laboratory conditions. At this stage, we deliberately avoid testing in complex real-world ecosystems to minimize potential ecological disturbance.

4.1.2 Ethical Concerns Related to This Project

Environmental Impact

- The robot body is made of hydrogel or biodegradable polymers. The selected materials are non-toxic and will not release microplastics or harmful substances into aquatic environments.
- We denote the environmental risk as the product of potential impact I and failure probability P_f:

  $$R = I \cdot P_f$$

  With careful material selection and extensive testing in lab conditions, we aim to keep $R \ll 1$, ensuring minimal ecological risk.
- The robot's actuation and propulsion systems are designed to minimize wake turbulence, reducing potential interference with planktonic or benthic species.

Privacy and Data Protection

- The onboard camera system is solely used for real-time navigation and control. No sensitive or personally identifiable information (PII) is captured.

- All captured images are anonymized and stored with hashed filenames. Data transmission between modules is encrypted using TLS.
- Ethical safeguards include:
  - **No secondary use of data** (e.g., for surveillance or unauthorized research).
  - **Data minimization**: Only frames necessary for navigation and detection are retained.

Testing and Safety in Natural Environments

- If the project advances to real aquatic field tests, we will seek approval from local environmental and wildlife authorities, such as the Environmental Protection Bureau or Marine Conservation Society.
- Before field deployment, all components will undergo:
  - **Sterilization procedures** to prevent contamination.
  - **Containment tests** to ensure no debris or chemicals are released.

4.2 Safety Considerations

Our project follows **ECE 445 Safety Guidelines** to ensure a safe working environment for both developers and the ecosystem where the robot operates. Below, we address potential safety concerns related to **electrical, mechanical, and environmental safety**.

4.2.1 Electrical Safety

- The system operates on **low-voltage DC power** (5–12 V), reducing the risk of electric shock.
- The Arduino Nano Every microcontroller controls four relays (model: LYCA005Y) through NPN transistors (Q1–Q4). Each relay switches external devices using isolated contacts.
- The LYCA005Y relay operates at 5V and has a coil resistance of:

  $$R_{\text{coil}} = 56\ \Omega$$

  which results in a coil current of:

  $$I_{\text{coil}} = \frac{5\ \text{V}}{56\ \Omega} \approx 89.3\ \text{mA}$$

  This current flows through the collector–emitter path of the NPN transistor and is sourced from the external 5V power supply—not the Arduino.

- The Arduino I/O pin drives the transistor base through a 220 Ω resistor. With a base–emitter voltage drop of approximately $V_{BE} = 0.7$ V, the base current is calculated as:

$$I_{\text{base}} = \frac{5.0 - 0.7}{220}\ \text{A} \approx 19.5\ \text{mA}$$

- According to the official specifications of the Arduino Nano Every, the maximum recommended continuous current per I/O pin is 20 mA, and the absolute maximum is 40 mA.
- Therefore, the actual base current of 19.5mA is within safe operating limits and does not exceed the 40mA threshold.
- The electrical design is safe under normal operation, and all I/O-driven loads remain within the current specifications of the microcontroller.
- Figure 26 illustrates the transistor-relay drive circuit and current paths.

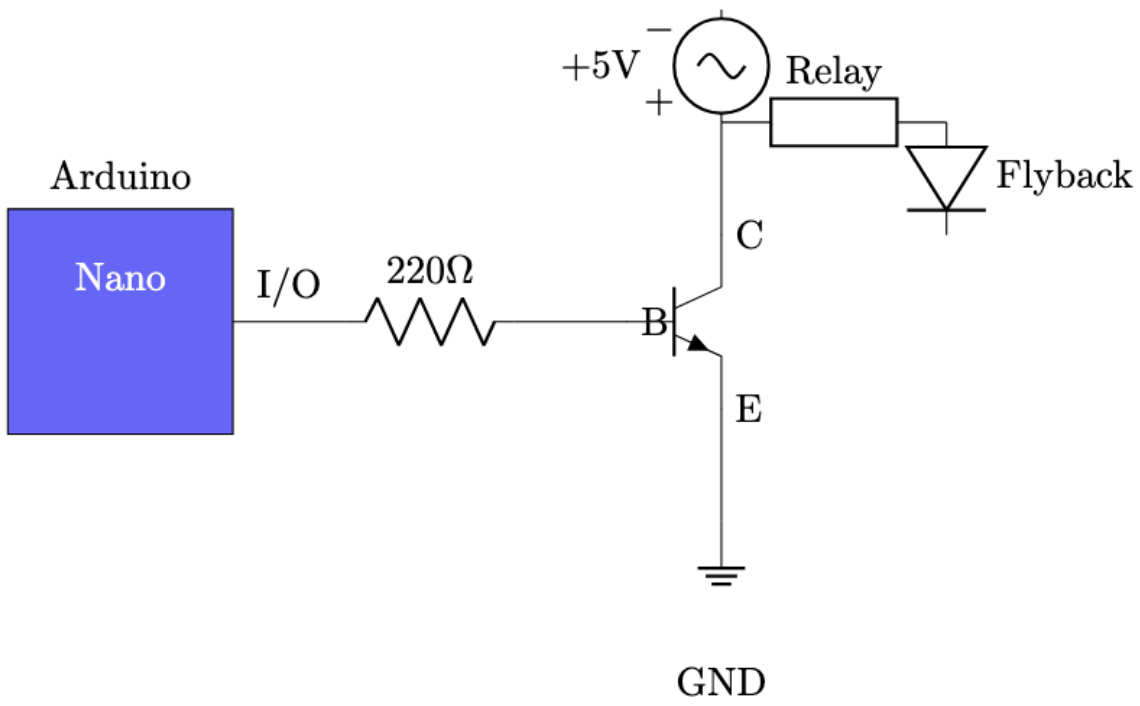

Figure 26: Transistor-based relay drive circuit showing current paths and calculation parameters.

4.2.2 Mechanical Safety

- The robot is entirely fabricated from soft hydrogel and elastomeric actuators, which inherently eliminate risks of cutting, pinching, or crushing during operation or accidental contact.

- The hydrogel materials used in the robot exhibit high stretchability, with maximum elongation ratios up to $\lambda = \frac{L}{L_0} = 3$, or 300%. Such high deformability ensures that even under accidental compression or tension, the structure absorbs energy and resists fracture.
- The Young's modulus E of the hydrogel is typically in the range of:

  $$E = 1 \sim 100 \text{ kPa}$$

  which is comparable to soft biological tissues (e.g., skin, muscle), making it inherently safe for contact with human or animal subjects.
- Actuation forces are limited by pressure-area relation:

  $$F = P \cdot A$$

  where internal pressure is capped at $P \leq 0.5 \text{ bar} = 5 \times 10^4 \text{ Pa}$, and the actuator contact area is $A \leq 1 \text{ cm}^2 = 10^{-4} \text{ m}^2$, giving:

  $$F \leq 5 \text{ N}$$

  which is well within the safe tactile force range (≤ 10 N) for human interaction.
- To ensure mechanical durability, all soft actuators and body structures undergo automated fatigue testing with over 10,000 actuation cycles. Failure points are logged and analyzed to prevent mechanical degradation over time.
- Furthermore, the robot's compliant nature enables it to deform upon contact, reducing potential impact forces. The contact stress can be estimated via:

  $$\sigma = \frac{F}{A} \leq \frac{5}{10^{-4}} = 5 \times 10^4 \text{ Pa} = 50 \text{ kPa}$$

  which remains below the pain threshold pressure for human skin (100 kPa), ensuring safe accidental contact.

4.2.3 Environmental Safety

- Hydrogel and elastomer materials are chosen for their proven biodegradability. Degradation half-life in aquatic environments is estimated as:

  $$t_{1/2} \approx 14\text{–}21 \text{ days}$$

  based on ASTM D6691 marine biodegradation standard.

- The robot's propulsion system (e.g., fin or jet) is tuned to generate low Reynolds number flows:

$$Re = \frac{\rho v L}{\mu} \approx 500\text{–}1000$$

  to minimize turbulent disturbance in aquatic environments.
- All lubricants, sealants, and coatings are certified non-toxic and water-stable.

4.2.4 Safety Plan

- **Prevention:** Software-in-the-loop (SIL) and hardware-in-the-loop (HIL) simulations are used to identify and isolate faults before hardware deployment.
- **Fail-Safe Mechanisms:**
  - Emergency kill-switch on the controller.
  - Watchdog timer to auto-disable actuation upon signal loss.
- **Protective Measures:**
  - Power regulators with thermal cutoff.
  - Floatation mechanism to bring the robot to surface in failure mode.
- **Training and Documentation:**
  - Lab members are required to complete a safety training module.
  - A full safety checklist is reviewed before every test.

4.2.5 High-Power Safety Example:

Although the instantaneous power during the initial charging process can be as high as:

$$P = \frac{V^2}{R} = \frac{7000^2}{29.7} \approx 1.65\ \text{MW},$$

this condition only lasts for a very short time, determined by the RC time constant. Given a capacitance of $C = 0.2603\ \text{nF}$ and resistance $R < 29.7\ \Omega$, the time constant is approximately:

$$\tau = RC < 29.7 \times 2.603 \times 10^{-10} \approx 7.73 \times 10^{-9}\ \text{s}\ (7.73\ \text{ns}),$$

which means the high power is delivered only during the nanosecond-scale charging transient.

Moreover, the total electrical charge stored in the EBSA is:

$$Q = C \cdot V = 2.603 \times 10^{-10} \cdot 7000 \approx 1.82\ \mu\text{C}.$$

This extremely small charge corresponds to very low stored energy, making the system intrinsically safe. Despite the use of high voltage, the low energy and short duration ensure minimal risk of electric shock or thermal hazard. Therefore, the high-voltage EBSA system is considered electrically safe for experimental use.

References

[1] S. Aracri, F. Giorgio-Serchi, G. Suaria, *et al.*, "Soft robots for ocean exploration and offshore operations: A perspective," *Soft Robotics*, vol. 8, no. 6, pp. 625–639, 2021, PMID: 33450174. DOI: 10.1089/soro.2020.0011. eprint: https://doi.org/10.1089/soro.2020.0011. [Online]. Available: https://doi.org/10.1089/soro.2020.0011.

[2] J. Yuh and M. West, "Underwater robotics," *Advanced Robotics*, vol. 15, no. 5, pp. 609–639, 2001. DOI: 10.1163/156855301317033595. eprint: https://doi.org/10.1163/156855301317033595. [Online]. Available: https://doi.org/10.1163/156855301317033595.

[3] J. Shintake, V. Cacucciolo, D. Floreano, and H. Shea, "Soft robotic grippers," *Adv. Mater.*, vol. 30, no. 29, p. 1 707 035, 2018. DOI: https://doi.org/10.1002/adma.201707035. eprint: https://onlinelibrary.wiley.com/doi/pdf/10.1002/adma.201707035. [Online]. Available: https://onlinelibrary.wiley.com/doi/abs/10.1002/adma.201707035.

[4] P. Polygerinos *et al.*, "Soft robotics: Review of fluid-driven intrinsically soft devices; manufacturing, sensing, control, and applications in human-robot interaction," *Adv. Eng. Mater.*, vol. 19, no. 12, p. 1 700 016, 2017. DOI: https://doi.org/10.1002/adem.201700016. eprint: https://onlinelibrary.wiley.com/doi/pdf/10.1002/adem.201700016. [Online]. Available: https://onlinelibrary.wiley.com/doi/abs/10.1002/adem.201700016.

[5] W.-S. Chu, K.-T. Lee, S.-H. Song, *et al.*, "Review of biomimetic underwater robots using smart actuators," *International Journal of Precision Engineering and Manufacturing*, vol. 13, no. 7, pp. 1281–1292, Jul. 2012, ISSN: 2005-4602. DOI: 10.1007/s12541-012-0171-7. [Online]. Available: https://doi.org/10.1007/s12541-012-0171-7.

[6] C. Lee, M. Kim, Y. J. Kim, *et al.*, "Soft robot review," *International Journal of Control, Automation and Systems*, vol. 15, no. 1, pp. 3–15, Feb. 2017, ISSN: 2005-4092. DOI: 10.1007/s12555-016-0462-3. [Online]. Available: https://doi.org/10.1007/s12555-016-0462-3.

[7] R. Pelrine, R. Kornbluh, Q. Pei, and J. Joseph, "High-speed electrically actuated elastomers with strain greater than 100%," *Science*, vol. 287, no. 5454, pp. 836–839, 2000. DOI: 10.1126/science.287.5454.836. eprint: https://www.science.org/doi/pdf/10.1126/science.287.5454.836. [Online]. Available: https://www.science.org/doi/abs/10.1126/science.287.5454.836.

[8] X. Li, D. Rao, M. Zhang, *et al.*, "A jelly-like artificial muscle for an untethered underwater robot," *Cell Reports Physical Science*, vol. 5, no. 5, May 2024, Publisher: Elsevier, ISSN: 2666-3864. DOI: 10.1016/j.xcrp.2024.101957. [Online]. Available: https://doi.org/10.1016/j.xcrp.2024.101957 (visited on 04/06/2025).

[9] G. Li, X. Chen, F. Zhou, *et al.*, "Self-powered soft robot in the Mariana Trench," en, *Nature*, vol. 591, no. 7848, pp. 66–71, Mar. 2021, Publisher: Nature Publishing Group, ISSN: 1476-4687. DOI: 10.1038/s41586-020-03153-z. [Online]. Available: https://www.nature.com/articles/s41586-020-03153-z (visited on 03/21/2025).

[10] A. O'Halloran, F. O'Malley, and P. McHugh, "A review on dielectric elastomer actuators, technology, applications, and challenges," *Journal of Applied Physics*, vol. 104, no. 7, p. 071 101, Oct. 2008, ISSN: 0021-8979. DOI: 10.1063/1.2981642. eprint: https:

//pubs.aip.org/aip/jap/article-pdf/doi/10.1063/1.2981642/15020155/071101_1_online.pdf. [Online]. Available: https://doi.org/10.1063/1.2981642.

[11] U. Gupta, L. Qin, Y. Wang, H. Godaba, and J. Zhu, "Soft robots based on dielectric elastomer actuators: A review," *Smart Materials and Structures*, vol. 28, no. 10, p. 103 002, Sep. 2019. DOI: 10.1088/1361-665X/ab3a77. [Online]. Available: https://dx.doi.org/10.1088/1361-665X/ab3a77.

[12] E. Hajiesmaili and D. R. Clarke, "Dielectric elastomer actuators," *Journal of Applied Physics*, vol. 129, no. 15, p. 151 102, Apr. 2021, ISSN: 0021-8979. DOI: 10.1063/5.0043959. eprint: https://pubs.aip.org/aip/jap/article-pdf/doi/10.1063/5.0043959/19887285/151102_1_5.0043959.pdf. [Online]. Available: https://doi.org/10.1063/5.0043959.

[13] X. Wang, S. K. Mitchell, E. H. Rumley, P. Rothemund, and C. Keplinger, "High-strain peano-hasel actuators," *Adv. Funct. Mater.*, vol. 30, no. 7, p. 1 908 821, 2020. DOI: https://doi.org/10.1002/adfm.201908821. eprint: https://onlinelibrary.wiley.com/doi/pdf/10.1002/adfm.201908821. [Online]. Available: https://onlinelibrary.wiley.com/doi/abs/10.1002/adfm.201908821.

[14] S. Zhang, X. Ke, Q. Jiang, H. Ding, and Z. Wu, "Programmable and reprocessable multifunctional elastomeric sheets for soft origami robots," *Sci. Robot.*, vol. 6, no. 53, eabd6107, 2021. DOI: 10.1126/scirobotics.abd6107. eprint: https://www.science.org/doi/pdf/10.1126/scirobotics.abd6107. [Online]. Available: https://www.science.org/doi/abs/10.1126/scirobotics.abd6107.

[15] T. Wang, H.-J. Joo, S. Song, W. Hu, C. Keplinger, and M. Sitti, "A versatile jellyfish-like robotic platform for effective underwater propulsion and manipulation," *Sci. Adv.*, vol. 9, no. 15, eadg0292, 2023. DOI: 10.1126/sciadv.adg0292. eprint: https://www.science.org/doi/pdf/10.1126/sciadv.adg0292. [Online]. Available: https://www.science.org/doi/abs/10.1126/sciadv.adg0292.

[16] N. Kellaris, V. G. Venkata, G. M. Smith, S. K. Mitchell, and C. Keplinger, "Peano-hasel actuators: Muscle-mimetic, electrohydraulic transducers that linearly contract on activation," *Sci. Robot.*, vol. 3, no. 14, eaar3276, 2018. DOI: 10.1126/scirobotics.aar3276. eprint: https://www.science.org/doi/pdf/10.1126/scirobotics.aar3276. [Online]. Available: https://www.science.org/doi/abs/10.1126/scirobotics.aar3276.

[17] J. Madden, N. Vandesteeg, P. Anquetil, *et al.*, "Artificial muscle technology: Physical principles and naval prospects," *IEEE J. Oceanic Eng.*, vol. 29, no. 3, pp. 706–728, 2004. DOI: 10.1109/JOE.2004.833135.

[18] Z. Ye, G. Yang, H. Dai, *et al.*, "Ocyropsis-inspired fast-swimming transparent soft robots," *Advanced Functional Materials*, vol. n/a, no. n/a, p. 2 421 522, DOI: https://doi.org/10.1002/adfm.202421522. eprint: https://advanced.onlinelibrary.wiley.com/doi/pdf/10.1002/adfm.202421522. [Online]. Available: https://advanced.onlinelibrary.wiley.com/doi/abs/10.1002/adfm.202421522.

[19] L. Tynan, U. Gunawardana, R. Liyanapathirana, *et al.*, "Review of electrohydraulic actuators inspired by the hasel actuator," *Biomimetics*, vol. 10, no. 3, 2025, ISSN: 2313-7673. DOI: 10.3390/biomimetics10030152. [Online]. Available: https://www.mdpi.com/2313-7673/10/3/152.

[20] E. Acome, S. K. Mitchell, T. G. Morrissey, *et al.*, "Hydraulically amplified self-healing electrostatic actuators with muscle-like performance," *Science*, vol. 359, no. 6371, pp. 61–65, 2018. DOI: 10.1126/science.aao6139. eprint: https://www.science.org/doi/pdf/10.1126/science.aao6139. [Online]. Available: https://www.science.org/doi/abs/10.1126/science.aao6139.

[21] S. Zhao and J. Yuh, "Experimental study on advanced underwater robot control," *IEEE Transactions on Robotics*, vol. 21, no. 4, pp. 695–703, 2005. DOI: 10.1109/TRO.2005.844682.

[22] S. Adam, L. Busoniu, and R. Babuska, "Experience replay for real-time reinforcement learning control," *IEEE Transactions on Systems, Man, and Cybernetics, Part C (Applications and Reviews)*, vol. 42, no. 2, pp. 201–212, Mar. 2012, ISSN: 1558-2442. DOI: 10.1109/TSMCC.2011.2106494.

[23] M. Waltz and K. Fu, "A heuristic approach to reinforcement learning control systems," *IEEE Transactions on Automatic Control*, vol. 10, no. 4, pp. 390–398, Oct. 1965, ISSN: 1558-2523. DOI: 10.1109/TAC.1965.1098193.

[24] K. Arulkumaran, M. P. Deisenroth, M. Brundage, and A. A. Bharath, "Deep reinforcement learning: A brief survey," *IEEE Signal Processing Magazine*, vol. 34, no. 6, pp. 26–38, Nov. 2017, ISSN: 1558-0792. DOI: 10.1109/MSP.2017.2743240.

[25] J. Schulman, F. Wolski, P. Dhariwal, A. Radford, and O. Klimov, *Proximal policy optimization algorithms*, 2017. arXiv: 1707.06347 [cs.LG]. [Online]. Available: https://arxiv.org/abs/1707.06347.

[26] P. I. Corke, "Visual control of robot manipulators – a review," in *Visual Servoing*, pp. 1–31. DOI: 10.1142/9789814503709_0001. eprint: https://www.worldscientific.com/doi/pdf/10.1142/9789814503709_0001. [Online]. Available: https://www.worldscientific.com/doi/abs/10.1142/9789814503709_0001.

[27] P. I. Corke *et al.*, *Visual Control of Robots: high-performance visual servoing*. Research Studies Press Taunton, UK, 1996.

[28] V. Francois-Lavet, P. Henderson, R. Islam, M. G. Bellemare, and J. Pineau, "An introduction to deep reinforcement learning," *Foundations and Trends® in Machine Learning*, vol. 11, no. 3, pp. 219–354, 2018, ISSN: 1935-8237, 1935-8245. DOI: 10.1561/2200000071. arXiv: 1811.12560[cs]. [Online]. Available: http://arxiv.org/abs/1811.12560 (visited on 04/07/2025).

[29] J. Schulman, F. Wolski, P. Dhariwal, A. Radford, and O. Klimov, *Proximal Policy Optimization Algorithms*, arXiv:1707.06347 [cs], Aug. 2017. DOI: 10.48550/arXiv.1707.06347. [Online]. Available: http://arxiv.org/abs/1707.06347 (visited on 03/11/2025).

[30] E. F. Moore, "Gedanken-experiments on sequential machines," in *Automata Studies*, Section: Automata Studies, Princeton University Press, Mar. 2, 2016, pp. 129–154, ISBN: 978-1-4008-8261-8. [Online]. Available: https://www.degruyterbrill.com/document/doi/10.1515/9781400882618-006/pdf?licenseType=restricted (visited on 04/07/2025).

[31] 3M Company, *Technical Data Sheet: 3M™ VHB™ Tape Specialty Tape 4905*, https://multimedia.3m.com/mws/media/2369629O/3m-vhb-tape-specialty-tape-4905-technical-data-sheet.pdf, Accessed: 2025-04-04, 2016.

[32] 3M Company, *Technical Data Sheet: 3M™ VHB™ Tape Specialty Tape 4910*, https://multimedia.3m.com/mws/media/2369649O/3m-vhb-tape-specialty-tape-4910-technical-data-sheet.pdf, Accessed: 2025-04-04, 2016.

[33] Dow Silicones Corporation, *Xiameter™ pmx-200 silicone fluid 0.65 cst – technical data sheet*, https://daltosur.com/media/documents/xiameter-pmx-200-silicone-fluid-065-csttds052022.pdf, Accessed: 2025-04-04, 2019.

[34] J. Mark, *Polymer Data Handbook*. New York: Oxford University Press, 1999, p. 424, Dielectric constant of trimethylsiloxy-terminated PDMS (0.65 cSt) is reported as approximately 2.2 at 25 °C over the frequency range 10^2-10^4 Hz., ISBN: 9780195107890. [Online]. Available: https://books.google.com/books?id=qFi5QgAACAAJ.

[35] J. Bouillon, C. Gravili, F. Pagès, J.-M. Gili, and F. Boero, *An Introduction to Hydrozoa*. Paris: Publications Scientifiques du Muséum, 2006.